Mon. Not. R. Astron. Soc. **362,** 1435–1450 (2005) doi:10.1111/j.1365-2966.2005.09415.x

Broad-band spectra of Cygnus X-1 and correlations between spectral characteristics

Askar Ibragimov,[1,2⋆] Juri Poutanen,[1⋆†] Marat Gilfanov,[3,4] Andrzej A. Zdziarski[5] and Chris R. Shrader[6]

[1]*Astronomy Division, PO Box 3000, FIN-90014 University of Oulu, Finland*
[2]*Kazan State University, Astronomy Department, Kremlyovskaya 18, 420008 Kazan, Russia*
[3]*Max-Planck-Institut für Astrophysik, Karl-Schwarzschild-Str. 1, 85740 Garching, Germany*
[4]*Space Research Institute, Russian Academy of Sciences, Profsoyuznaya 84/32, 117810 Moscow, Russia*
[5]*Centrum Astronomiczne im. M. Kopernika, Bartycka 18, 00-716 Warszawa, Poland*
[6]*Laboratory for High-Energy Astrophysics, NASA Goddard Space Flight Center, Greenbelt, MD 20771, USA*

Accepted 2005 July 6. Received 2005 May 24; in original form 2005 February 21

ABSTRACT

We present the results of the spectral analysis of 42 simultaneous broad-band *Ginga*–OSSE and *RXTE*–OSSE observations of Cygnus X-1 carried out in 1991 and 1996–1999. The broad-band spectra from 3 to ∼1000 keV can be well described by the thermal Comptonization model with reflection from the cold disc, with an additional soft component visible below 10 keV. The relative contribution of this component to the total energy flux appears to be higher in the spectra with larger reflection amplitude and steeper photon index of the thermal Comptonized component. We consider a number of physically realistic models to describe the shape of the $E \lesssim 10$ keV excess. The additional soft component can result from thermal Comptonization by electrons with a low Compton parameter, or can be a part of a non-thermal, power-law-like emission extending above 1 MeV.

We study correlations between parameters obtained from the spectral fits with different models. We confirm a general correlation between the photon index Γ and the amplitude of reflection R. We find that simple phenomenological models (such as power law plus Compton reflection) applied to the narrow band (3–20 keV) data overestimated the values of R and Γ, although the simple models did rank correctly the spectra according to R and Γ, as demonstrated in the original publications on this subject.

The dynamic corona model provides a satisfactory description of the observed correlation, while the hot inner disc models have problems in reproducing it quantitatively. On the other hand, in the context of the dynamic corona model it is difficult to understand correlations with the timing characteristics, which seems natural in the hot disc scenario. We do not find significant correlation between the electron temperature and other spectral parameters, while the optical depth of the hot medium seems to decrease when the spectrum becomes softer. It is also shown that spectral parameters are well correlated with the timing characteristics of the source.

Key words: accretion, accretion discs – black hole physics – stars: individual: Cygnus X-1 – gamma-rays: observations – X-rays: binaries.

1 INTRODUCTION

Matter accreting on to a black hole, whether supermassive in Seyfert galaxies or stellar mass in Galactic X-ray binaries, releases most of its gravitational energy in the form of X-rays deep in the potential well. Accretion may proceed in a number of regimes. The accreting gas can approach the black hole in a disc-like configuration (Shakura & Sunyaev 1973) if the gravitational energy is effectively transported away in the form of radiation, or in the form of an almost spherical flow if the energy exchange mechanism between protons (carrying most of the energy) and electrons is inefficient (Shapiro, Lightman & Eardley 1976; Ichimaru 1977; Narayan, Mahadevan &

⋆E-mail: askar.ibragimov@oulu.fi (AI); juri.poutanen@oulu.fi (JP)
†Corresponding Fellow, NORDITA, Copenhagen.

Quataert 1998). Magnetic fields can play an important role transporting a large fraction of the total available energy and dissipating it in a rarefied medium (corona) above the disc (Galeev, Rosner & Vaiana 1979; Tout & Pringle 1992; Svensson & Zdziarski 1994; Beloborodov 1999a; Miller & Stone 2000). However, every model is based on a number of assumptions that include prescriptions for the viscosity, the vertical distribution of the energy release through the flow, the energy transport mechanisms, etc. Given the difficulties in the accretion physics, observations should help in choosing among the different possibilities as well as guiding theoreticians in the right direction.

Cygnus X-1, one of the best studied black hole binaries (BHBs), has served as an accretion disc laboratory since the end of the 1960s. The most dramatic observed phenomena are the spectral state transitions occurring every few years, when the source, typically emitting most of its energy at about 100 keV in the hard state, switches to a soft state consisting of a prominent ∼1-keV blackbody and a power-law-like tail. The hard state spectrum was believed to originate from thermal Comptonization in a hot electron cloud (Shapiro et al. 1976; Ichimaru 1977; Sunyaev & Trümper 1979; Sunyaev & Titarchuk 1980). The blackbody-looking soft-state spectrum was associated with the optically thick accretion disc (Shakura & Sunyaev 1973), while the origin of ∼100-keV emission in that state was not discussed much, because the detailed spectrum was not available.

During the last decade, the quality of the X/γ-spectra increased dramatically improving our knowledge as well as producing many new questions. In the hard state, the spectrum turns out to be rather complicated containing a number of components. Thanks to the broad-band coverage by *Ginga* and *CGRO* (and later by *ASCA*, *RXTE* and *BeppoSAX*), and advances in modelling of Comptonization at mildly relativistic temperatures (Coppi 1992; Poutanen & Svensson 1996), the parameters of the electron cloud where Comptonization takes place were determined to a high accuracy. In Cyg X-1, the electron temperature of $kT_{\rm e} \simeq 100 \pm 50$ keV and Thomson optical depth of $\tau \simeq 1$–2 were found to be typical (Zdziarski et al. 1996, 1997; Gierliński et al. 1997; Poutanen 1998; Di Salvo et al. 2001; Frontera et al. 2001; Zdziarski & Gierliński 2004). The Compton reflection bump, a signature of the presence of cold matter in the vicinity of the X-ray emitting source, was discovered (Done et al. 1992; Ebisawa et al. 1996; Gierliński et al. 1997). The blackbody associated with the cooler accretion disc (Balucińska & Hasinger 1991; Balucińska-Church et al. 1995; Ebisawa et al. 1996) and an additional soft excess at a few keV of unknown origin further complicate spectral decomposition (Di Salvo et al. 2001; Frontera et al. 2001). A high-energy excess at >500 keV discovered by *CGRO* (McConnell et al. 1994; Ling et al. 1997) gives some clues about the presence of non-thermal particles in the source.

The X/γ-ray soft-state spectrum has been studied extensively by simultaneous observations with *ASCA*, *RXTE*, *BeppoSAX* and *CGRO* during the summer of 1996. In addition to the dominating blackbody, a long power-law-like tail extending up to 10 MeV was discovered (McConnell et al. 2002). The high-energy spectrum could be well described by single Compton scattering off electrons having a nearly power-law distribution (Poutanen 1998; Poutanen & Coppi 1998; Gierliński et al. 1999, hereafter G99; Frontera et al. 2001). The Compton reflection was stronger than in the hard state, which was interpreted as a change in the geometry of the system, from the hot inner flow in the hard state to the standard Shakura–Sunyaev disc with a non-thermal corona in the soft state (Bisnovatyi-Kogan & Blinnikov 1977; Ichimaru 1977; Poutanen, Krolik & Ryde 1997; Li & Miller 1997; Esin et al. 1998; Poutanen & Coppi 1998). Evaporation and condensation of the gas can provide a physical basis for the change of the transition radius between standard disc and hot inner flow (Meyer, Liu & Meyer-Hofmeister 2000; Różańska & Czerny 2000). A smaller reflection fraction in the hard state, however, can be explained by a beaming of the primary emission away from the disc due to mildly relativistic motion of the emitting plasma (ejection model; see Beloborodov 1999a,b; Malzac, Beloborodov & Poutanen 2001, hereafter MBP01). In order to distinguish among different possibilities, it is necessary to compare model predictions with other observational facts.

A few, well separated in time, broad-band spectra do not give us a good picture about relations between different components, such as, for example, Comptonized continuum and the reflection bump. It is possible to study these relations on a larger data set in a narrower energy band. Zdziarski, Lubiński & Smith (1999, hereafter ZLS99) and Gilfanov, Churazov & Revnivtsev (1999, hereafter GCR99) analysing data from *Ginga* and *RXTE*, respectively, have shown that the photon spectral slope of the Comptonized emission, Γ, is strongly correlated with the amplitude of Compton reflection component, $R = \Omega/2\pi$, where Ω is the solid angle the cool material covers as viewed from the source of primary X-rays. This correlation exists for individual BHBs and Seyfert galaxies as well as in a sample of sources (see also Gilfanov, Churazov & Revnivtsev 2000; Revnivtsev, Gilfanov & Churazov 2001). Zdziarski et al. (2003) studied possible statistical and systematic effects and concluded that the correlation exists beyond any reasonable doubt. Similar correlation also exists for Fourier-frequency resolved spectra, i.e. those corresponding to the variability in a given range of Fourier frequencies (Revnivtsev, Gilfanov & Churazov 1999).

The observed correlation provides extremely important clues to the geometry of the accreting material and can be used for testing the theoretical model. The fact that Γ and R are correlated is a natural consequence of coexistence of the cold media (accretion disc) and a hot Comptonizing gas in the vicinity of the black hole. The cold material acts as a source of seed photons for Comptonization and, at the same time, reflects and reprocesses the hard radiation produced in the hot gas.

The cold disc with the hot inner flow model naturally produces the correlation if there is an overlap between hot and cold phases (Poutanen et al. 1997; ZLS99). However, the Γ–R dependence observed in BHBs can be quantitatively reproduced only if the ratio of the seed photon temperature, $kT_{\rm seed}$, to the electron temperature is about 10^{-4} (ZLS99; Gilfanov et al. 2000). For $kT_{\rm e} \sim 100$ keV, this gives $kT_{\rm seed} \sim 10$ eV, which is an order of magnitude smaller than the disc temperature in BHBs and closer to that expected from Seyferts. For $kT_{\rm seed} \sim 300$ eV, the spectra are too hard for the given reflection fraction. In this model, the spectral slope is an extremely steep function of the overlap between the corona and the disc, while the reflection varies very little (Beloborodov 2001). Intrinsic dissipation in the disc can make spectra softer for the given reflection, but then the spectral slope will be an even steeper function of the overlap. Values of reflection larger than 1 sometimes observed in Seyferts also cannot be explained. On the other hand, all the data can be well described by the ejection model with the correct $kT_{\rm seed}$ (Beloborodov 1999a,b; MBP01).

The problem is that theoretical models try to reproduce the best-fitting Γ and R, which are subject to a number of systematic effects. The photon index and, especially, the strength of the Compton reflection depend crucially on the spectral shape of the underlying continuum and description of the reflection physics (see detailed discussion in Zdziarski et al. 2003). All the papers above, where this correlation was studied, assumed the underlying spectrum to be

a power law. Because the Comptonization spectrum has a cut-off at high energies, it gives fewer incident photons that are available for reflection (Weaver, Krolik & Pier 1998; Malzac & Petrucci 2002; Perola et al. 2002), and thus the fitted R would be larger. Fitting an exponentially cut-off power law to the broad-band data (e.g. Matt 2001; Perola et al. 2002) does not improve the situation, because this model does not reproduce well the shape of the Comptonization continuum (Malzac & Petrucci 2002; Zdziarski et al. 2003). The approximate treatment of ionization could be another source of errors.

As discussed above, the spectra of BHBs are rather complex having a number of components, and it is not possible to resolve different spectral components (e.g. thermal Comptonization and soft excess) in the narrow energy range of an instrument such as *RXTE*/Proportional Counter Array (PCA) or *Ginga*/Large Area Proportional Counter (LAC). There is a danger that different components overlap in that energy band producing effectively a power law of one index while in reality the slope of the primary emission could be rather different. The resulting reflection amplitude could be also influenced significantly. Thus, in order to obtain actual Γ and R to be used in theoretical models, the analysis of broad-band data with physical models (such as Comptonization) is absolutely necessary.

Additional sources of information are the width of the fluorescent Fe Kα line at 6.4 keV and the frequencies of the quasi-periodic oscillations (QPOs) that were also observed to correlate with the reflection fraction and the spectral slope (GCR99; Gilfanov et al. 2000). This seems to be consistent with the variations of the inner cold disc radius. Not much data exist on the variability of the electron temperature and Thomson optical depth of the Comptonizing source, which can provide information about the nature of the emitting plasma (electron–proton or electron–positron). It would be of interest to determine how the optical depth changes with the bolometric flux, because this can help in distinguishing the accretion mode the flow is in.

In this paper, we analyse a large set of simultaneous broad-band spectra. Four observations of Cyg X-1 by *Ginga*/LAC and *CGRO*/OSSE from 1991 as well as 38 observations by *RXTE*/PCA, *RXTE*/HEXTE and *CGRO*/OSSE from 1996–1999 are studied in detail. For the spectral analysis, we use physically motivated Comptonization models and study correlations between model parameters such as the spectral slope of the primary Comptonization continuum, the reflection amplitude, the width of the Fe line, the electron temperature of the hot gas, and its Thomson optical depth.

2 OBSERVATIONS AND DATA ANALYSIS

The observation log is presented in Table 1. Data reduction for *RXTE* has been carried out using LHEASOFT 5.3.1 software; PCA responses were generated using PCARSP v. 10.1 and HEXTE responses were used from 2000 May 26. In PCA data reduction, all five PCUs were taken into account, when possible. If not all PCUs were turned on, we use PCUs 0, 2 and 3. Judging from the Crab data, these two PCU configurations produce similar spectral slopes. Systematic errors of 0.5 per cent were added in quadrature to the PCA data. *CGRO*/OSSE spectra were prepared by adding per-orbit data (average exposure 2–5 ks), with total exposure up to 12 h and contemporary PCA observation in the middle of the period. The systematic error in OSSE spectra varies from 3 per cent at 50 keV to 0.3 per cent at 300 keV. The stability of the OSSE spectra was checked using hardness ratios (154–282/52–154 keV) for per-orbit spectra being added. If orbital spectra within 12 h were apparently different, we lowered the total integration time to include only similar data.

We used PCA data from 3 to 20 keV, HEXTE data from 20–25 to 200 keV and OSSE data from 50 to 1000 keV. In addition, four *Ginga*/LAC and OSSE simultaneous observations from 1991, previously studied by Gierliński et al. (1997), were also analysed. The *Ginga*/LAC data are available from 1.7 keV, but we decided to use exactly the same energy interval as covered by the PCA. For the spectral analysis, we use XSPEC 11.3.1k (Arnaud 1996).

The spectra may be separated into two groups based on the difference of their photon index (see Fig. 1). Spectra from 1991 and 1997, represented by observation 6, have $\Gamma \sim 1.6$ (usual for the hard state) and those from 1999 (observations 25 and 31) have $\Gamma \sim 1.8$–2.2; hereafter, we call the corresponding state flat (because the spectrum is nearly flat in the $EF_{\rm E}$ plot). The spectra from 1996 and 1998 are close to the hardest ones from 1999. We do not consider here the broad-band soft-state spectra, for which a similar analysis has been performed by G99 and Frontera et al. (2001).

3 SPECTRAL ANALYSIS

In order to describe the observed broad-band spectra, we use the following models:

(0) power law (without or with an exponential cut-off) and Compton reflection (PEXRAV model; Magdziarz & Zdziarski 1995);

(1) two thermal Comptonization models and reflection, with the soft excess also modelled by thermal Comptonization;

(2) thermal Comptonization with reflection plus a non-thermal Comptonization corresponding to the soft state spectrum.

We use the EQPAIR code (Coppi 1999; G99) for modelling thermal and non-thermal Comptonization. All models include also a Gaussian line at 6.4 keV and interstellar absorption with column density $N_{\rm H}$, which we find often larger than the value of 0.6×10^{22} cm^{-2} (derived from the reddening towards the companion star; see Balucińska-Church et al. 1995). To avoid unreasonably low values of this parameter, its low limit was set to 0.5×10^{22} cm^{-2}. The presented uncertainties are given at a 90 per cent confidence level for a single parameter ($\Delta\chi^2 = 2.71$). Fluxes, unless stated otherwise, correspond to the range covering all the model emission.

3.1 Power law and reflection model in the 3–20 keV data

The spectra of Cyg X-1 clearly show correlations between reflection amplitude and the spectral index (GCR99, ZLS99). Detailed analysis confirms (Zdziarski et al. 2003) that the extent of correlation is much larger than typical errors in the best-fitting parameters. However, because the PCA spectrum falls in a quite narrow energy interval, it is difficult to distinguish between various spectral components that may form an 'effective' power law. Therefore, it is not certain that the values for Γ and R obtained from the simple power-law/reflection fits indeed correspond to the actual physical situation.

Still, in order to compare our results with those of previous analysis, we have performed fits similar to those presented in ZLS99 and GCR99. We later compare them to the results obtained with more physical models (see Section 4.4). We use the XSPEC model PHABS*(PEXRAV+GAUSSIAN) (model 0), i.e. a power law with the photon index, Γ, and Compton reflection with the relative strength, R (Magdziarz & Zdziarski 1995), accompanied by a Gaussian fluorescence Fe Kα line (characterized by the relativistic smearing width σ and the equivalent width), all absorbed by interstellar material of

Table 1. Observation log.

No	*RXTE* ObsID	*Ginga* or PCA exposure[a] (s)	HEXTE exposure[b] (s)	Date	Time (UT)	*CGRO* VP	OSSE exposure (s)	Time (UT)
				1991 hard state				
G1		2304		June 6	00:18–02:10	02	4121	00:03–02:11
G2		888		June 6	04:43–06:29	02	4040	04:29–06:51
G3		2828		June 6	11:03–14:25	02	5975	10:43–14:32
G4		1272		June 6	20:22–20:44	02	1629	20:02–20:33
				1996 flat state				
1	10238-01-08-000	14 592	5083	March 26	10:12–17:36	516.5	17 538	07:22–20:01
2	10238-01-07-000	8446	2922	March 27	23:06–05:20	516.5	23 018	20:20–07:47
3	10238-01-06-00	11 455	3713	March 29	11:43–17:33	516.5	21 868	08:24–21:06
4	10238-01-05-000	10 397	3524	March 30	19:54–01:58[c]	516.5	24 153	16:51–04:12[c]
				1997 hard state				
5	10239-01-01-00	9095	–	Feb 2	20:13–02:03	612.5	47 864	16:53–04:52[c]
6	10238-01-03-00	6441	1938	Feb 3	19:30–22:06	612.5	44 530	14:38–02:36[c]
7	30158-01-01-00	1175	809	Dec 10	07:08–08:30	705	7552	02:55–12:46
8	30158-01-02-00	2012	823	Dec 11	07:06–08:45	705	12 004	04:11–14:05
9	30158-01-03-00	2027	706	Dec 14	08:48–10:20	705	11 599	03:09–11:35
10	30158-01-05-00	2614	901	Dec 15	05:26–07:09	705	16 721	23:31–11:18[c]
11	30158-01-06-00	3210	941	Dec 17	00:40–02:05	706	13 017	20:13–07:32[d]
12	30157-01-02-00	2309	784	Dec 18	07:07–08:16	706	9924	01:49–08:46
13	30158-01-07-00	2275	766	Dec 20	07:11–08:29	706	11 847	02:46–12:52
14	30158-01-08-00	2581	878	Dec 21	05:28–07:05	706	14 924	00:51–12:31[c]
15	30157-01-03-00	2846	860	Dec 24	21:24–23:03	707	10 127	21:36–03:18[c]
16	30161-01-01-000	13 244	4136	Dec 28	13:56–21:03	707	13 717	11:33–00:24[c]
17	30158-01-12-00	2836	916	Dec 30	03:52–05:00	707	8979	23:49–07:57[d]
				1998 flat state				
18	30155-01-01-020	10 027	3897	Dec 23	00:07–05:58	804	2957	21:52–09:00[d]
19	30155-01-02-00	9625	3399	Dec 28	01:40–07:09	804	5124	23:14–10:29[d]
20	30161-01-03-01	9863	3371	Dec 28	13:08–18:37	804	5289	11:50–21:31
21	40100-01-04-00	8472	–	Dec 29	01:37–05:57	804	5476	22:51–10:08[d]
22	40100-01-05-00	8476	–	Dec 30	01:38–05:57	804	5288	22:30–09:46[d]
23	40100-01-06-00	7245	–	Dec 31	03:12–07:11	804	5552	23:44–11:00[d]
				1999 flat state				
24	40101-01-09-00	2405	665	Oct 5	18:39–19:45	831.5	29 605	15:04–01:12[c]
25	40101-01-11-00	731	165	Oct 6	19:22–20:03	831.5	25 960	14:39–00:50[c]
26	40101-01-12-00	865	–	Oct 7	07:10–07:40	831.5	28 389	03:08–12:55
27	40101-01-15-00	741	218	Oct 8	08:07–08:48	831.5	31 014	04:20–14:35
28	40101-01-16-00	757	215	Oct 9	09:41–10:22	831.5	33 770	03:55–15:48
29	40099-01-20-01	1228	354	Oct 12	17:33–19:56	831.5	37 186	12:11–01:23[c]
30	40100-01-11-01	4300	–	Oct 28	10:46–15:12	832	19 559	06:16–17:46
31	40099-01-22-00	1444	520	Nov 8	14:44–15:25	832	17 504	09:52–21:28
32	40099-01-23-01	3084	1453	Nov 23	15:26–17:32	834.5	8734	15:14–21:54
33	40100-01-13-01	770	–	Nov 24	20:08–20:59	834.5	19 652	14:51–02:13[c]
34	40100-01-14-02	479	–	Nov 25	20:05–20:56	834.5	16 683	14:24–01:47[c]
35	40100-01-15-03	1729	–	Nov 26	21:40–22:32	834.5	24 372	17:11–04:33[c]
36	40100-01-16-02	1448	–	Nov 27	19:59–20:50	834.5	19 063	15:13–02:34[c]
37	40100-01-17-03	1902	–	Nov 28	21:32–22:27	834.5	10 309	19:19–00:28[c]
38	40100-01-18-03	1961	–	Nov 29	21:29–22:25	834.5	19 999	16:03–03:19[c]

[a]The deadtime-corrected exposure. [b]HEXTE cluster 0 exposure. Symbol '–' means that no HEXTE data are available. [c]The observation finished on the following day. [d]The observation started on the previous day.

column density $N_{\rm H}$. Hereafter, we assume the disc inclination of $i = 50^\circ$ and neutral reflector.

The fit results are presented in Table 2. Only the low-energy 3–20 keV (*RXTE*/PCA and *Ginga*/LAC) data were fitted, and therefore we did not apply any high-energy cut-off to the power law. We find that the correlations between spectral parameters (see Fig. 2) are similar to the results of GCR99.

As shown in Section 3.2, there is a likely overlap of different spectral components in the PCA energy range. Therefore, model 0 cannot represent a good approach for physical interpretations for the spectra. Taking into account also the OSSE data and including an exponential cut-off in the model, we can model the joint data only very roughly, with $\chi^2/{\rm dof} \sim 2$. This is likely to be due to the shape of the exponential cut-off (which is assumed in PEXRAV) being substantially different from the shape of the cut-off of thermal Comptonization (see, for example, Zdziarski et al. 2003). This provides an argument against utilizing simple phenomenological models in the analysis of BHB spectra.

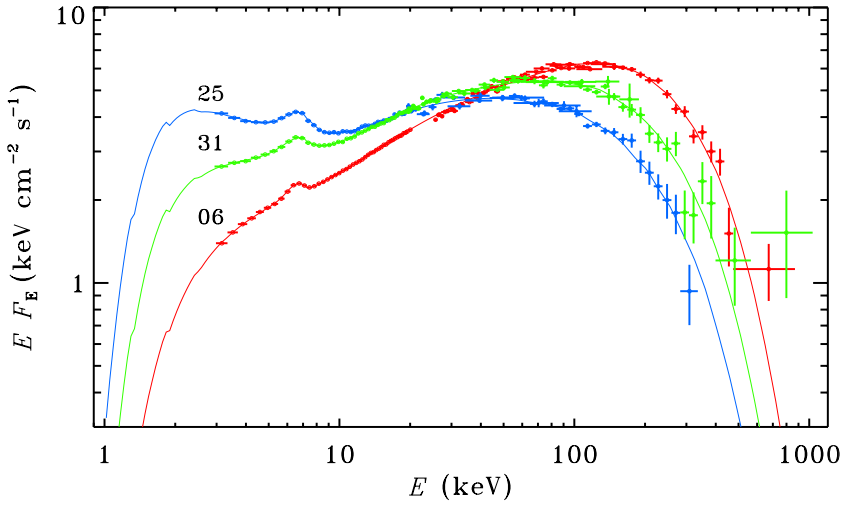

Figure 1. Broad-band spectra of Cyg X-1 as observed by *RXTE* and OSSE (with the respective observation number from Table 1) and the best-fitting models. Theoretical curves represent model 1 for observations 6, 25 and 31 (see Section 3). All of the figures are colour in the online version of the paper on *Synergy*.

3.2 Comptonization model and broad-band spectra

The hard-state spectra are well described by thermal Comptonization (Gierliński et al. 1997; Poutanen 1998; Frontera et al. 2001), with a weak soft excess. To describe Comptonization we use the XSPEC model EQPAIR (see Coppi 1999; G99). The spectrum of seed photons is from a pseudo-Newtonian accretion disc (see G99). The parameters of emission are expressed through the compactness

$$\ell = \frac{L\sigma_{\rm T}}{\mathcal{R}m_{\rm e}c^3}, \qquad (1)$$

where L is the source luminosity, $\mathcal{R}$ is the radius of the emitting spherical cloud, and $\sigma_{\rm T}$ is the Thomson cross-section. We consider here thermal plasma. The model is characterized by the following parameters: $\ell_{\rm s}$ is the compactness of soft seed photons (assumed here to be 1); $\ell_{\rm h}/\ell_{\rm s}$ is the ratio of the dimensionless energy dissipation rate in a hot cloud to $\ell_{\rm s}$; $kT_{\rm max}$ is the maximal colour temperature of the disc (at 9.5 gravitational radii, $R_{\rm g} = GM/c^2$, or at the inner radius of the disc, if it is cut-off at larger value); $\tau_{\rm p}$ is the Thomson optical depth corresponding to the ions; R is the reflection amplitude. Because there are large (∼25 per cent at 1σ) errors on $kT_{\rm max}$, we decided to fix it at the common value of 200 eV. The model computed the coronal temperature, $kT_{\rm e}$, and the total optical depth, τ, from the background electrons and produced $e^{\pm}$ pairs self-consistently from the energy and pair balance. For the assumed compactness, pair production is negligible for all considered spectra, and thus the resulting total optical depth $\tau = \tau_{\rm p}$. In the fits, we assume the inner disc radius of $6R_{\rm g}$ (this parameter only has an effect on the relativistic smearing of the reflected component, which could hardly be resolved with present energy resolution).

The normalization of EQPAIR, corresponding to the disc component, is $f_{\rm c}M^2\cos i/(D^2\beta_{\rm c}{}^4)$, where $f_{\rm c}$ is the covering factor, M is the black hole mass in units of the solar mass, D is the distance to the source in units of kpc, and $\beta_{\rm c}$ is the ratio of the colour temperature to the effective temperature.

At low energies, the effect of the interstellar absorption is clearly visible. The addition of an additional soft component leads to further improvement of the fits. Such soft excesses were observed in both the hard state by Di Salvo et al. (2001) and in a flat state (similar to that analysed here) by Frontera et al. (2001) in *BeppoSAX* data. However, this component, whose nature we address below, is relatively weak in the case of 1991 and 1997 (observations G1–G4, 05–17) hard-state data. The spectra observed in 1996, 1998 and 1999 (observations 1–4, 18–38) appear similar in overall shape to those of the hard state, but are significantly softer (see Fig. 2). The soft excess in the flat state is stronger.

We stress that the requirement of an additional soft excess is implied only by the joint PCA/HEXTE/OSSE data, because the PCA data cover a too narrow energy range. Even if the actual spectrum in the PCA 3–20 keV band is not a power law but is, for example, concave, a good fit with a power law plus reflection (model 0) can be still achieved. However, the real strength of Compton reflection can be significantly different.

Because the data require an additional component only in a relatively narrow range (∼3–10 keV), the parameters of the soft excess cannot be constrained accurately. Below we consider a number of physically realistic scenarios of its nature. In each of the considered models, we restrict the parameters controlling its spectral shape to values that make its flux significant only at low energies, and we fit only its normalization. These fits allow us to completely describe the broad-band spectra and to constrain the parameters of main continuum.

3.2.1 *High temperature of the optically thick disc*

The additional component may, in principle, be emitted by the hottest part of the optically thick disc provided its temperature is high enough. We find that the spectra of the observations 1–4, 18–38 can be well fitted with $kT_{\rm max} \sim 1$ keV. However, Di Salvo et al. (2001) have shown that the spectral decomposition of the *BeppoSAX* data of Cyg X-1 in the hard state requires the presence of both the soft blackbody disc photons (with $kT_{\rm max} \simeq 0.1$–0.2 keV) and an additional soft excess component. Therefore, we consider this model to be not appropriate.

3.2.2 *Hybrid model*

We also tried to apply hybrid thermal + non-thermal EQPAIR model to the spectra. Most of the data require nearly non-thermal injection and the resulting spectrum becomes a power law directed by the PCA part of the spectrum. Because the observed hard tail is not a power law, large reflection appears to mimic the cut-off region, but it is still not enough to describe both the soft excess below 10 keV

Table 2. The best-fitting parameters for model 0 (fitted to the low-energy *Ginga* and *RXTE*/PCA data only).

No.	$N_{\rm H}$ (10^{22} cm^{-2})	Γ	R	σ (keV)	EW (eV)	χ^2/dof
			1991			
G1	$0.5^{+1.2}_{-0}$	$1.63^{+0.09}_{-0.03}$	$0.39^{+0.19}_{-0.08}$	$0.46^{+0.81}_{-0.46}$	134^{+47}_{-66}	3/11
G2	$0.5^{+1.2}_{-0}$	$1.62^{+0.09}_{-0.03}$	$0.37^{+0.18}_{-0.09}$	$0.58^{+0.93}_{-0.58}$	152^{+54}_{-73}	4/11
G3	$1.3^{+1.3}_{-0.8}$	$1.60^{+0.10}_{-0.07}$	$0.26^{+0.17}_{-0.13}$	$0.60^{+0.95}_{-0.60}$	142^{+77}_{-75}	3/11
G4	$1.4^{+1.2}_{-0.9}$	$1.69^{+0.09}_{-0.08}$	$0.41^{+0.19}_{-0.16}$	$0.42^{+0.97}_{-0.42}$	82^{+36}_{-60}	5/12
			1996			
01	1.2 ± 0.2	1.80 ± 0.02	0.51 ± 0.05	0.68 ± 0.16	96 ± 19	24/43
02	0.6 ± 0.2	1.79 ± 0.02	0.48 ± 0.05	0.80 ± 0.12	148 ± 20	20/43
03	0.7 ± 0.2	1.80 ± 0.02	0.48 ± 0.04	0.72 ± 0.12	138 ± 19	20/43
04	1.2 ± 0.2	1.89 ± 0.02	0.66 ± 0.05	0.87 ± 0.16	112 ± 19	24/43
			1997			
05	1.3 ± 0.3	1.65 ± 0.02	0.25 ± 0.04	$0.40^{+0.22}_{-0.40}$	66 ± 20	19/39
06	1.2 ± 0.3	1.65 ± 0.02	0.24 ± 0.04	$0.38^{+0.19}_{-0.33}$	76 ± 20	27/39
07	1.0 ± 0.3	1.71 ± 0.02	0.35 ± 0.05	$0.52^{+0.21}_{-0.26}$	79 ± 22	16/39
08	1.0 ± 0.3	1.69 ± 0.02	0.29 ± 0.04	$0.44^{+0.19}_{-0.24}$	86 ± 21	35/39
09	1.2 ± 0.3	1.71 ± 0.02	0.36 ± 0.05	$0.56^{+0.21}_{-0.25}$	82 ± 22	26/39
10	1.2 ± 0.2	1.69 ± 0.02	0.32 ± 0.05	$0.43^{+0.20}_{-0.27}$	77 ± 20	22/39
11	1.2 ± 0.2	1.70 ± 0.02	0.32 ± 0.04	$0.35^{+0.20}_{-0.35}$	69 ± 19	15/39
12	3.1 ± 0.2	1.72 ± 0.02	0.38 ± 0.05	$0^{+0.42}_{-0}$	32 ± 12	23/39
13	2.1 ± 0.3	1.71 ± 0.02	0.37 ± 0.05	$0.30^{+0.55}_{-0.30}$	56 ± 19	21/39
14	1.1 ± 0.3	1.70 ± 0.02	0.37 ± 0.05	$0.43^{+0.20}_{-0.29}$	78 ± 21	21/39
15	2.1 ± 0.3	1.70 ± 0.02	0.35 ± 0.05	$0.15^{+0.53}_{-0.15}$	41 ± 18	17/39
16	2.1 ± 0.2	1.69 ± 0.02	0.41 ± 0.05	$0.17^{+0.43}_{-0.17}$	57 ± 16	22/39
17	2.7 ± 0.3	1.71 ± 0.02	0.36 ± 0.05	$0.03^{+2.79}_{-0.03}$	37 ± 17	19/39
			1998			
18	1.2 ± 0.2	1.87 ± 0.02	0.54 ± 0.05	0.73 ± 0.16	99 ± 20	19/39
19	1.2 ± 0.2	1.84 ± 0.02	0.48 ± 0.05	0.71 ± 0.17	95 ± 20	19/39
20	1.2 ± 0.2	1.85 ± 0.02	0.50 ± 0.05	0.71 ± 0.17	96 ± 20	17/39
21	1.1 ± 0.2	1.83 ± 0.02	0.47 ± 0.05	0.71 ± 0.17	93 ± 20	14/39
22	0.7 ± 0.2	1.83 ± 0.02	0.47 ± 0.05	0.69 ± 0.14	123 ± 21	20/39
23	0.7 ± 0.2	1.82 ± 0.02	0.46 ± 0.05	0.72 ± 0.13	135 ± 21	17/39
			1999			
24	$0.5^{+0.1}_{-0}$	2.09 ± 0.01	0.89 ± 0.07	0.93 ± 0.12	203 ± 23	28/33
25	$0.5^{+0.1}_{-0}$	2.30 ± 0.02	1.38 ± 0.16	1.12 ± 0.16	249 ± 34	48/33
26	$0.5^{+0.1}_{-0}$	2.23 ± 0.01	1.15 ± 0.10	1.09 ± 0.13	247 ± 27	43/33
27	$0.5^{+0.2}_{-0}$	2.05 ± 0.01	0.81 ± 0.08	0.95 ± 0.14	188 ± 25	14/33
28	0.7 ± 0.3	2.05 ± 0.03	0.84 ± 0.10	0.82 ± 0.15	161 ± 26	32/33
29	$0.5^{+0.1}_{-0}$	2.01 ± 0.01	0.74 ± 0.07	0.91 ± 0.15	185 ± 25	22/33
30	$0.5^{+0.1}_{-0}$	2.20 ± 0.01	1.07 ± 0.07	1.03 ± 0.11	237 ± 22	27/33
31	$0.5^{+0.2}_{-0}$	1.94 ± 0.02	0.61 ± 0.06	0.82 ± 0.13	170 ± 22	25/33
32	1.1 ± 0.3	1.85 ± 0.03	0.50 ± 0.06	0.54 ± 0.23	79 ± 22	20/33
33	$0.7^{+0.3}_{-0.2}$	1.87 ± 0.03	0.53 ± 0.07	0.63 ± 0.19	113 ± 26	30/33
34	$0.6^{+0.3}_{-0.1}$	1.86 ± 0.03	0.47 ± 0.08	0.61 ± 0.19	125 ± 28	14/33
35	$0.5^{+0.2}_{-0}$	1.88 ± 0.02	0.52 ± 0.05	0.65 ± 0.13	141 ± 18	25/33
36	$0.5^{+0.2}_{-0}$	1.88 ± 0.02	0.55 ± 0.06	0.72 ± 0.14	156 ± 22	25/33
37	1.2 ± 0.3	1.92 ± 0.03	0.62 ± 0.07	0.68 ± 0.18	109 ± 24	27/33
38	1.2 ± 0.3	1.98 ± 0.03	0.77 ± 0.08	0.78 ± 0.16	125 ± 24	39/33

and the hard tail, in which the systematic difference between the data and the model remains. Therefore, we ruled out this model.

3.2.3 Two thermal Comptonization components

The soft component can be described by additional thermal Comptonization (Di Salvo et al. 2001; Frontera et al. 2001). We use the model 1, PHABS(COMPTT+EQPAIR+GAUSSIAN), where EQPAIR gives the main Comptonization and COMPTT (Titarchuk 1994) the additional soft component. Because the parameters of the soft excess are rather weakly constrained by our data, we fixed the parameters of COMPTT at $kT_{\rm e} = 20$ keV and $\tau = 1$. Such a model produces a soft power law that does not extend to very high energies. This model fitted to the data of observation 24 is shown in Fig. 3. In

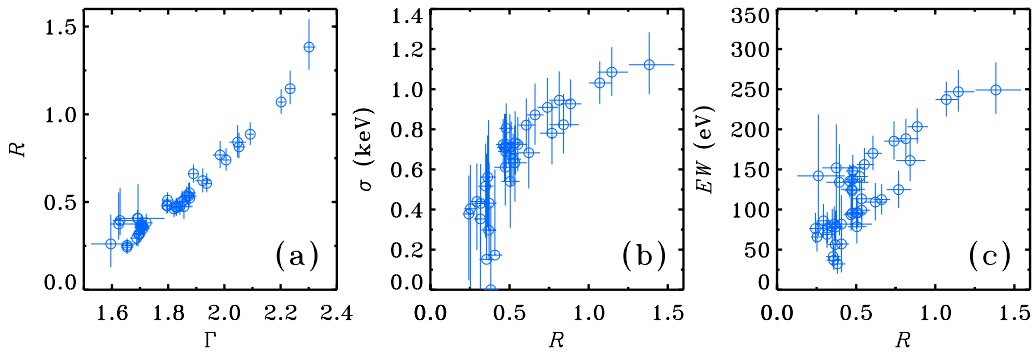

Figure 2. Correlations between parameters for model 0 (PEXRAV). (a) The reflection amplitude, R, versus the photon spectral index, Γ. (b) The relativistic smearing Gaussian width σ versus reflection R. (c) The Fe Kα 6.4-keV line equivalent width versus R.

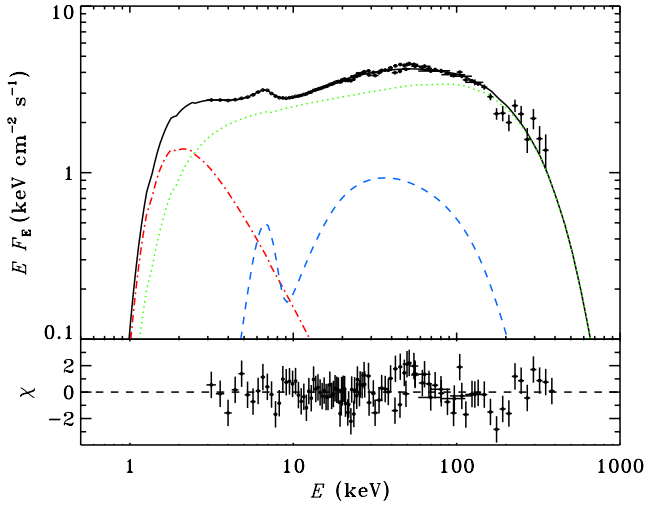

Figure 3. The model spectrum with two thermal Comptonization components (model 1, Section 3.2.3) fitted to the *RXTE*+OSSE observation 24 (from 1999). The spectral components of the fit are shown by the dotted (green), dot-dashed (red) and dashed (blue) curves, which correspond to the main thermal Comptonization continuum, the additional thermal Comptonization with $kT_e = 20$ keV and $\tau = 1$, and the Compton reflection including the Fe line, respectively. The solid (black) curve shows the total spectrum. The lower panel shows the residuals of the fit.

spite of its simplicity, it yields a relatively good description of the data.

The fit parameters are given in Table 3, and the dependences between various model parameters are shown in Fig. 4. We also quote the values of the spectral index Γ of the power law obtained from the least-squares fitting of the logarithm of the intrinsic model flux at a logarithmic energy grid in the 2–10 keV range (chosen to enable comparison with the results of other papers).

The meaning of the normalization of EQPAIR has been described in Section 3.2. Substituting $f_c = 1$, $M = 10\,M_\odot$, $i = 50°$, $D = 2.0$ kpc (see references in G99; Frontera et al. 2001) and $\beta_c = 1.7$ (Shimura & Takahara 1995), we expect the normalization of $\simeq$1.92. The lower normalization of the obtained fits (see Table 3) is caused either by a larger $\beta_c \sim 1.77$–1.98 or by a smaller covering factor f_c. A slightly smaller, than the assumed disc temperature of 200 eV, can also reduce the normalization. On the other hand, some flat-state normalizations are larger than the expected value of 1.92. This cannot be explained by changing f_c (a smaller covering factor can only reduce the normalization), but could be a result of somewhat larger inner disc radius or larger temperature. The largest observed normalizations correspond to $kT_{max} \sim 220$–245 eV.

We see that there is a clear anticorrelation between the strength of the soft component and the hardness of spectrum expressed in terms of ℓ_h/ℓ_s. There is also a correlation between τ and ℓ_h/ℓ_s. The reflection amplitude is correlated with the Fe line equivalent width and anticorrelated with ℓ_h/ℓ_s (while at high values of ℓ_h/ℓ_s the anticorrelation possibly breaks down).

The electron temperature kT_e is a calculated parameter and no errors on it can be obtained from fitting. However, we estimated its 1σ limits using its extremal values within the uncertainties of the parameters controlling spectral shape, i.e. ℓ_h/ℓ_s and τ. This estimation gives us a possible conservative error on kT_e of about 15 keV for both models 1 and 2. Taking this into account, no correlations between kT_e–flux and $kT_e - \ell_h/\ell_s$ are apparent.

3.2.4 Thermal continuum and non-thermal Comptonization component

As an alternative to the second thermal Compton component, we consider here addition of a non-thermal Comptonization component. We find that such a non-thermal component can describe both the soft excess and the MeV non-thermal tail observed in hard states by the Compton Telescope (COMPTEL; McConnell et al. 2002), while neither of these components can be described by the main thermal Compton emission. This model fitted to the spectrum 24 is shown in Fig. 5. Note that the COMPTEL data are shown for illustration only and were not taken into account in the fitting. The used model 2 consists of PHABS(EQPAIR+EQPAIR+GAUSSIAN), in which the second EQPAIR component produces the non-thermal spectrum. In EQPAIR, the available power is supplied in part into heating electrons and in part into their acceleration, with the resulting steady-state electron distribution calculated self-consistently. The compactness corresponding to the acceleration is hereafter denoted as ℓ_{nth}. Then the relative fraction of the input power going into the non-thermal acceleration is ℓ_{nth}/ℓ_h, where ℓ_h (as before) corresponds to the total rate of energy dissipation in the plasma.

For that additional component, we assumed that all the available power goes into non-thermal acceleration, i.e. $\ell_{nth}/\ell_h = 1$. Note that the resulting self-consistent electron distribution is not purely non-thermal but hybrid, i.e. it does contain a low-energy Maxwellian heated by Compton and Coulomb interactions. We further assume $R = 0$, the power-law index of the accelerated electrons of $\Gamma_{inj} = 2.4$ (see Poutanen & Coppi 1998; G99; Frontera et al. 2001; McConnell et al. 2002), the minimum and maximum Lorentz factors of the power law of $\gamma_{min} = 1.3$ and $\gamma_{max} = 1000$, respectively,

Table 3. The best-fitting parameters for model 1.

Obs.	$N_{\rm H}^{a}$	$\ell_{\rm h}/\ell_{\rm s}$	τ	R	σ	EW	N^{b}	$F_{\rm tot}^{c}$	$F_{\rm add}^{d}$	$kT_{\rm e}{}^{e}$	Γ^{f}	χ^2/dof
G1	$1.1^{+0.8}_{-0.6}$	$13.8^{+0.9}_{-0.7}$	$1.39^{+0.07}_{-0.08}$	$0.38^{+0.04}_{-0.03}$	$0.67^{+0.32}_{-0.34}$	189^{+57}_{-51}	$1.36^{+0.05}_{-0.06}$	5.32	0.11	90	1.62	49/73
G2	1.3 ± 0.8	$15.6^{+1.3}_{-0.8}$	$1.58^{+0.12}_{-0.05}$	$0.35^{+0.04}_{-0.05}$	$0.87^{+0.36}_{-0.31}$	235^{+75}_{-63}	$1.63^{+0.06}_{-0.09}$	7.24	0.24	82	1.59	58/74
G3	1.4 ± 0.2	$14.0^{+0.9}_{-1.6}$	$1.34^{+0.08}_{-0.20}$	$0.26^{+0.06}_{-0.04}$	$0.60^{+0.92}_{-0.60}$	151^{+54}_{-47}	$1.13^{+0.10}_{-0.04}$	4.18	0	94	1.62	53/73
G4	$2.0^{+0.7}_{-0.9}$	13.4 ± 1.8	$1.36^{+0.29}_{-0.30}$	$0.26^{+0.09}_{-0.08}$	$0.63^{+0.41}_{-0.31}$	132^{+57}_{-48}	$1.04^{+0.14}_{-0.11}$	3.83	0.14	90	1.63	53/73
01	2.6 ± 0.2	$10.3^{+0.4}_{-0.1}$	$1.31^{+0.06}_{-0.03}$	$0.27^{+0.02}_{-0.01}$	$1.00^{+0.16}_{-0.13}$	173^{+26}_{-20}	$1.99^{+0.03}_{-0.09}$	7.32	1.26	86	1.68	501/478
02	2.1 ± 0.3	$9.76^{+0.18}_{-0.24}$	$1.32^{+0.02}_{-0.03}$	$0.29^{+0.01}_{-0.02}$	$1.11^{+0.12}_{-0.13}$	240^{+25}_{-27}	$2.50^{+0.06}_{-0.04}$	8.83	1.56	83	1.69	531/493
03	$2.2^{+0.3}_{-0.2}$	$10.2^{+0.1}_{-0.2}$	$1.47^{+0.05}_{-0.03}$	0.26 ± 0.02	$1.02^{+0.14}_{-0.13}$	227^{+28}_{-29}	2.18 ± 0.03	8.04	1.49	75	1.68	542/506
04	2.9 ± 0.2	$8.77^{+0.18}_{-0.14}$	$1.38^{+0.03}_{-0.02}$	0.31 ± 0.01	1.12 ± 0.11	215^{+23}_{-19}	$2.85^{+0.05}_{-0.07}$	10.0	2.44	77	1.71	529/493
05	$1.6^{+0.4}_{-0.3}$	$11.8^{+1.2}_{-0.4}$	$1.09^{+0.16}_{-0.03}$	0.22 ± 0.02	$0.48^{+0.22}_{-0.23}$	77^{+18}_{-16}	$1.30^{+0.03}_{-0.09}$	4.46	0.08	110	1.65	61/73
06	1.8 ± 0.4	$12.8^{+0.3}_{-0.5}$	$1.29^{+0.03}_{-0.08}$	$0.19^{+0.02}_{-0.01}$	$0.54^{+0.19}_{-0.21}$	96 ± 19	$1.05^{+0.04}_{-0.02}$	3.99	0.19	95	1.64	374/402
07	$1.9^{+0.3}_{-0.4}$	12.0 ± 0.4	$1.24^{+0.13}_{-0.07}$	0.22 ± 0.02	$0.75^{+0.19}_{-0.23}$	121^{+24}_{-27}	$1.54^{+0.04}_{-0.06}$	5.80	0.52	96	1.65	367/415
08	$2.0^{+0.3}_{-0.4}$	$11.9^{+0.3}_{-0.4}$	$1.41^{+0.03}_{-0.04}$	$0.20^{+0.02}_{-0.01}$	$0.68^{+0.19}_{-0.21}$	118^{+21}_{-22}	$1.47^{+0.04}_{-0.02}$	5.43	0.46	84	1.65	404/415
09	2.3 ± 0.3	$12.0^{+0.4}_{-0.2}$	$1.41^{+0.03}_{-0.06}$	0.23 ± 0.02	$0.85^{+0.20}_{-0.18}$	131^{+26}_{-21}	$1.56^{+0.03}_{-0.04}$	5.98	0.62	84	1.65	350/415
10	$1.6^{+0.5}_{-0.4}$	$11.3^{+0.3}_{-0.4}$	$1.18^{+0.08}_{-0.05}$	$0.24^{+0.02}_{-0.01}$	$0.56^{+0.19}_{-0.18}$	102^{+21}_{-18}	$1.43^{+0.02}_{-0.04}$	4.92	0.25	99	1.66	301/334
11	4.1 ± 0.3	$11.6^{+0.4}_{-0.5}$	$1.19^{+0.06}_{-0.03}$	0.23 ± 0.02	$0.41^{+0.74}_{-0.41}$	54^{+18}_{-17}	1.53 ± 0.04	5.72	0.58	99	1.65	193/236
12	4.2 ± 0.3	$11.8^{+0.6}_{-0.5}$	$1.20^{+0.10}_{-0.03}$	$0.23^{+0.02}_{-0.01}$	$0.43^{+0.78}_{-0.41}$	55^{+20}_{-17}	$1.52^{+0.04}_{-0.06}$	5.77	0.61	99	1.65	202/238
13	$2.5^{+1.0}_{-0.8}$	12.8 ± 0.4	$1.45^{+0.05}_{-0.03}$	0.22 ± 0.02	$0.58^{+0.24}_{-0.18}$	106^{+19}_{-20}	$1.45^{+0.04}_{-0.03}$	5.74	0.47	83	1.63	369/411
14	2.2 ± 0.3	$12.4^{+0.4}_{-0.3}$	1.34 ± 0.03	0.24 ± 0.02	$0.74^{+0.19}_{-0.17}$	126^{+23}_{-19}	$1.58^{+0.03}_{-0.04}$	6.25	0.63	90	1.64	397/415
15	3.2 ± 0.3	13.6 ± 0.5	$1.26^{+0.11}_{-0.04}$	0.19 ± 0.02	$0.60^{+0.35}_{-0.30}$	75^{+27}_{-19}	$1.29^{+0.03}_{-0.04}$	5.51	0.57	99	1.62	201/244
16	3.4 ± 0.3	13.7 ± 0.2	1.61 ± 0.04	0.24 ± 0.01	$0.55^{+0.19}_{-0.16}$	98^{+19}_{-14}	1.47 ± 0.02	6.53	0.76	76	1.62	446/402
17	3.8 ± 0.3	$12.9^{+0.6}_{-0.4}$	$1.33^{+0.15}_{-0.10}$	$0.19^{+0.02}_{-0.03}$	$0.60^{+0.29}_{-0.38}$	73 ± 21	$1.25^{+0.02}_{-0.05}$	5.12	0.55	92	1.63	345/415
18	2.5 ± 0.3	8.13 ± 0.15	$1.23^{+0.02}_{-0.03}$	$0.28^{+0.02}_{-0.01}$	$0.98^{+0.13}_{-0.11}$	182^{+23}_{-21}	2.32 ± 0.04	7.09	1.41	84	1.73	512/489
19	2.7 ± 0.3	$9.43^{+0.23}_{-0.09}$	$1.61^{+0.04}_{-0.03}$	0.21 ± 0.02	$1.02^{+0.15}_{-0.12}$	182^{+25}_{-21}	$1.67^{+0.02}_{-0.03}$	5.87	1.29	66	1.69	457/502
20	2.6 ± 0.3	$9.14^{+0.20}_{-0.09}$	$1.45^{+0.03}_{-0.06}$	$0.24^{+0.01}_{-0.02}$	$1.00^{+0.15}_{-0.12}$	182^{+26}_{-20}	$1.79^{+0.02}_{-0.03}$	6.11	1.29	73	1.70	472/502
21	2.6 ± 0.4	$9.91^{+2.16}_{-2.68}$	$1.36^{+0.59}_{-0.43}$	$0.20^{+0.11}_{-0.14}$	$0.94^{+0.18}_{-0.14}$	161^{+46}_{-23}	$1.83^{+0.56}_{-0.42}$	6.52	1.28	81	1.68	46/73
22	$2.1^{+0.3}_{-0.4}$	$8.96^{+2.38}_{-2.05}$	$1.19^{+0.43}_{-0.55}$	$0.24^{+0.08}_{-0.13}$	0.90 ± 0.12	188^{+25}_{-19}	$2.13^{+0.58}_{-0.55}$	6.86	1.21	90	1.71	45/73
23	2.0 ± 0.4	$8.57^{+1.55}_{-1.42}$	$1.29^{+0.25}_{-0.65}$	$0.26^{+0.14}_{-0.09}$	$0.89^{+0.12}_{-0.11}$	192^{+30}_{-20}	$2.14^{+0.58}_{-0.16}$	6.57	1.10	81	1.72	43/73
24	$1.6^{+0.3}_{-0.2}$	$5.43^{+0.68}_{-0.19}$	$1.08^{+0.13}_{-0.03}$	0.36 ± 0.03	$0.99^{+0.09}_{-0.08}$	337^{+28}_{-26}	$1.85^{+0.06}_{-0.27}$	4.71	1.46	83	1.82	389/409
25	1.5 ± 0.2	$4.70^{+0.57}_{-0.29}$	$1.04^{+0.17}_{-0.06}$	$0.36^{+0.04}_{-0.06}$	$0.98^{+0.08}_{-0.07}$	395^{+33}_{-30}	$2.46^{+0.14}_{-0.24}$	6.51	2.71	81	1.85	355/409
26	1.3 ± 0.3	$4.08^{+0.92}_{-0.49}$	$0.89^{+0.25}_{-0.14}$	$0.40^{+0.08}_{-0.09}$	1.01 ± 0.07	382^{+28}_{-28}	$2.54^{+0.29}_{-0.42}$	5.44	1.92	90	1.89	48/67
27	1.8 ± 0.3	5.95 ± 0.30	$1.10^{+0.05}_{-0.06}$	0.33 ± 0.03	1.02 ± 0.10	305 ± 30	$2.19^{+0.10}_{-0.09}$	5.92	1.81	84	1.80	386/409
28	$1.7^{+0.2}_{-0.3}$	$5.75^{+0.35}_{-0.50}$	$1.21^{+0.06}_{-0.16}$	$0.33^{+0.06}_{-0.04}$	$0.98^{+0.09}_{-0.08}$	335^{+31}_{-27}	1.74 ± 0.16	4.71	1.52	75	1.81	389/409
29	1.6 ± 0.3	$6.01^{+0.32}_{-0.24}$	$1.09^{+0.05}_{-0.04}$	0.33 ± 0.03	$0.99^{+0.11}_{-0.10}$	295^{+30}_{-29}	$1.98^{+0.07}_{-0.09}$	5.06	1.28	85	1.80	394/409
30	$0.9^{+0.2}_{-0.3}$	$2.71^{+1.06}_{-0.23}$	$0.46^{+0.26}_{-0.19}$	$0.62^{+0.08}_{-0.05}$	0.97 ± 0.08	328^{+19}_{-25}	$4.06^{+0.48}_{-0.15}$	5.67	1.46	141†	1.93	52/67
31	1.7 ± 0.3	$6.74^{+0.32}_{-0.39}$	$1.09^{+0.06}_{-0.14}$	$0.29^{+0.04}_{-0.03}$	0.93 ± 0.11	253^{+27}_{-26}	$1.91^{+0.11}_{-0.09}$	5.10	1.12	89	1.77	390/409
32	2.4 ± 0.3	$9.38^{+0.37}_{-0.40}$	$1.37^{+0.10}_{-0.08}$	$0.22^{+0.03}_{-0.02}$	0.83 ± 0.15	151^{+22}_{-25}	1.49 ± 0.06	5.08	1.01	79	1.70	393/409
33	$2.1^{+0.2}_{-0.6}$	$7.94^{+0.56}_{-1.26}$	$1.23^{+0.09}_{-0.24}$	$0.27^{+0.07}_{-0.02}$	$0.83^{+0.15}_{-0.19}$	179^{+33}_{-32}	$1.93^{+0.29}_{-0.10}$	5.76	1.16	84	1.73	62/67
34	$1.5^{+0.3}_{-0.5}$	$7.08^{+0.35}_{-0.89}$	$1.08^{+0.13}_{-0.19}$	$0.29^{+0.07}_{-0.04}$	$0.74^{+0.17}_{-0.18}$	174 ± 31	$1.83^{+0.25}_{-0.11}$	4.64	0.67	92	1.76	43/67
35	$1.4^{+0.3}_{-0.4}$	$7.05^{+0.53}_{-0.73}$	$1.08^{+0.11}_{-0.16}$	$0.30^{+0.06}_{-0.04}$	0.78 ± 0.11	206^{+25}_{-23}	$2.03^{+0.19}_{-0.12}$	5.26	0.85	91	1.76	40/67
36	$1.6^{+0.4}_{-0.6}$	$7.46^{+0.73}_{-1.24}$	$1.07^{+0.15}_{-0.20}$	$0.32^{+0.06}_{-0.05}$	$0.88^{+0.12}_{-0.17}$	230^{+27}_{-39}	$1.92^{+0.30}_{-0.14}$	5.35	0.96	94	1.75	62/64
37	$3.3^{+1.3}_{-1.3}$	$6.52^{+1.11}_{-1.01}$	$1.04^{+0.22}_{-0.21}$	$0.35^{+0.06}_{-0.07}$	$0.98^{+0.26}_{-0.23}$	179^{+31}_{-42}	$2.02^{+0.30}_{-0.23}$	5.53	1.39	92	1.78	40/62
38	$3.2^{+0.6}_{-1.2}$	$6.24^{+0.67}_{-0.72}$	$0.96^{+0.14}_{-0.13}$	0.37 ± 0.05	$0.96^{+0.19}_{-0.18}$	199 ± 28	$2.29^{+0.25}_{-0.18}$	6.33	1.80	98	1.78	41/62

[a]Hydrogen column density, in units of 10^{22} cm^{-2}. [b]Normalization of the EQPAIR model component. [c]The unabsorbed total model flux, in units of 10^{-8} erg cm^{-2} s^{-1}. [d]The unabsorbed model flux of the COMPTT component, in units of 10^{-8} erg cm^{-2} s^{-1}. [e]Temperature of the emitting plasma in keV (for the EQPAIR component). [f]Photon spectral index of the EQPAIR component in the 2–10 keV range.

$kT_{\rm max}$ equal to that of the main component, $\ell_{\rm h}/\ell_{\rm s} = 1$, and $\tau_{\rm p} = 1$. No pair production is required, and τ is found to be equal to $\tau_{\rm p}$.

The best-fitting parameters are presented in Table 4 and correlations between them are shown in Figs 6 and 11. The normalization of the thermal EQPAIR component corresponds to $\beta_{\rm c} = 1.63$–2.01, values similar to those obtained with model 1. The strength of the additional (non-thermal) component is again clearly anticorrelated with the spectral hardness. The anticorrelation between R and $\ell_{\rm h}/\ell_{\rm s}$ is apparent and corresponds to the R–Γ correlation that we discuss in Section 4.4. The values of R and the Fe line equivalent width are well correlated and can be approximated by a linear function

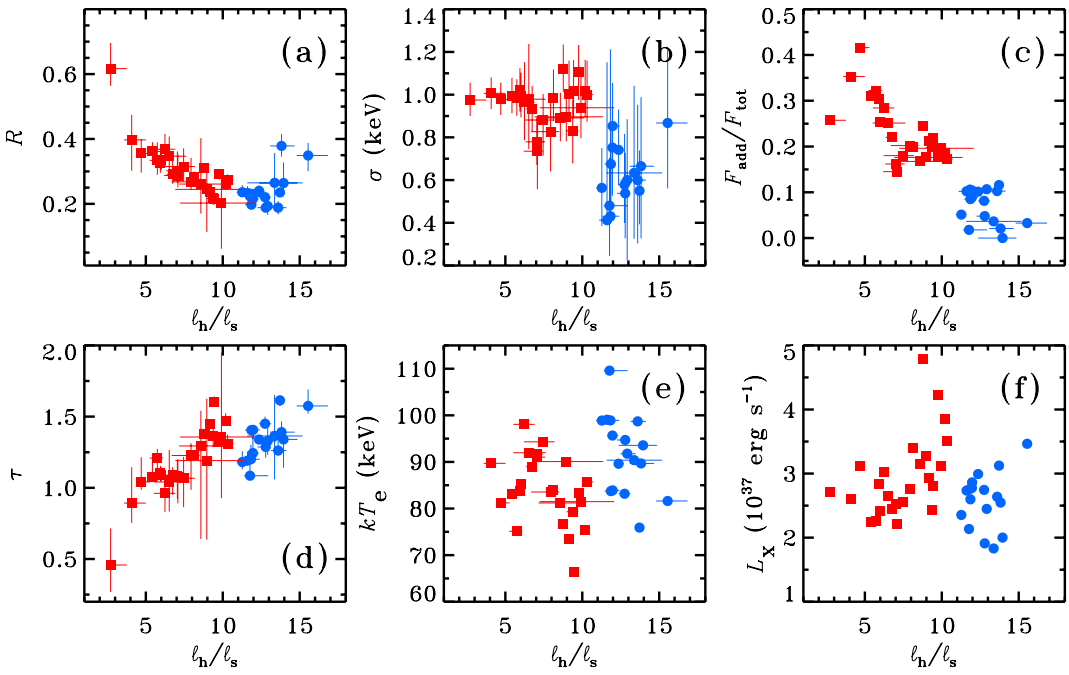

Figure 4. Dependences of the spectral parameters for model 1 (Section 3.2.3) fitted to the 1991 and 1997 (blue filled circles) and the 1996, 1998 and 1999 data (red filled squares) on the Compton amplification factor of the main Comptonization component $\ell_{\rm h}/\ell_{\rm s}$. (a) The reflection fraction R; (b) the relativistic smearing Gaussian width σ at 6.4 keV; (c) ratio of the additional thermal Comptonization flux to the total flux; (d) Thomson optical depth of the main Comptonization continuum component τ; (e) electron temperature of the main Comptonization component $kT_{\rm e}$; (f) total luminosity of the Comptonizing cloud (assuming $D = 2$ kpc).

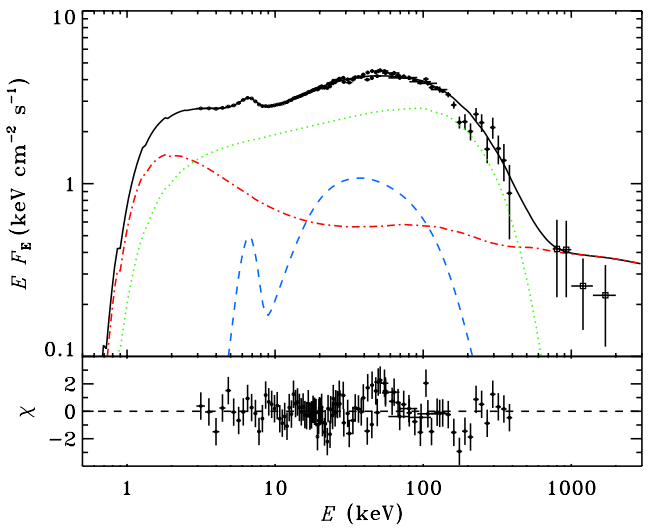

Figure 5. The model spectrum with the thermal and non-thermal Comptonization components (model 2, Section 3.2.4) fitted to the *RXTE*+OSSE observation 24 (from 1999) together with the COMPTEL (McConnell et al. 2002) hard-state data (marked by squares). The spectral components of the fit are shown by the dotted (green), dot-dashed (red) and dashed (blue) curves, which correspond to the main thermal Comptonization continuum, the additional non-thermal Comptonization and the Compton reflection including the Fe line, respectively. The solid curve shows the total spectrum. The lower panel shows the residuals of the fit.

passing through zero (see Fig. 11c). Again, there is a correlation between τ and $\ell_{\rm h}/\ell_{\rm s}$. The electron temperature does not seemingly depend on the hardness, but the spread becomes smaller at larger $\ell_{\rm h}/\ell_{\rm s}$ where $kT_{\rm e} \sim 90$ keV.

4 DISCUSSION

4.1 Absorption

As noted in Section 3, the hydrogen column density $N_{\rm H}$ was free in our fits. We find that our data require absorption significantly larger than $0.6 \pm 0.2 \times 10^{22}$ cm^{-2}, which is derived from the reddening towards the companion star (Balucińska-Church et al. 1995).

Cyg X-1 is known to show X-ray dips in its light curve, caused by obscuration by the stellar wind from the companion star. During dips, the absorption increases up to $N_{\rm H} = 20 \times 10^{22}$ cm^{-2}. The absorption shows strong orbital phase dependence with maximal column density around phase 0, when companion star is in front of the black hole (Balucińska-Church et al. 2000; Feng & Cui 2002). We plotted the fitted values of $N_{\rm H}$ versus Cyg X-1 orbital phase (see Fig. 7), using the ephemeris with the time of the primary minimum at 50234.79 MJD and the period of 5.599829 d (LaSala et al. 1998; Brocksopp et al. 1999). We see a good correlation of $N_{\rm H}$ with the orbital phase, which indicates that variable absorption can indeed be caused by the companion's wind obscuring the X-rays from the black hole.

We note that because our models are relatively complicated in the range of 3–10 keV (consisting of absorption, Comptonization together with the seed photon emission and a soft excess), and also the PCA energy range is affected by absorption rather weakly, it is difficult to determine the exact values of $N_{\rm H}$, even though the derived values of the parameter are in the range quoted by other authors and its relative changes are quite remarkable.

4.2 Spectral variability patterns

Using *CGRO*/BATSE and *RXTE*/ASM data, Zdziarski et al. (2002) showed that Cyg X-1 has two types of variability: changes of

Table 4. The best-fitting parameters for model 2.

Obs.	$N_{\rm H}{}^a$	$\ell_{\rm h}/\ell_{\rm s}$	τ	R	σ	EW	N^b	$F^c_{\rm tot}$	$F^d_{\rm add}$	$kT_{\rm e}{}^e$	Γ^f	χ^2/dof
G1	$0.9^{+0.5}_{-0.4}$	$14.2^{+1.1}_{-0.9}$	1.41 ± 0.08	0.40 ± 0.04	$0.61^{+0.32}_{-0.38}$	182^{+59}_{-52}	1.29 ± 0.09	5.32	0.21	90	1.62	49/73
G2	$1.0^{+0.5}_{-0.6}$	$16.4^{+2.1}_{-1.2}$	$1.62^{+0.17}_{-0.08}$	0.37 ± 0.05	$0.78^{+0.34}_{-0.32}$	210^{+68}_{-60}	$1.50^{+0.12}_{-0.20}$	8.23	0.93	81	1.58	56/74
G3	$1.4^{+0.4}_{-0.2}$	$14.0^{+0.9}_{-1.7}$	$1.35^{+0.08}_{-0.21}$	$0.26^{+0.07}_{-0.03}$	$0.58^{+0.93}_{-0.58}$	144^{+57}_{-50}	$1.12^{+0.10}_{-0.06}$	4.19	0.01	93	1.62	53/73
G4	$1.6^{+0.5}_{-0.6}$	$13.8^{+2.9}_{-1.9}$	$1.37^{+0.34}_{-0.30}$	$0.30^{+0.09}_{-0.08}$	$0.56^{+0.95}_{-0.58}$	122^{+55}_{-48}	$0.97^{+0.13}_{-0.15}$	3.81	0.23	91	1.62	53/73
01	2.0 ± 0.2	11.4 ± 0.3	$1.39^{+0.02}_{-0.04}$	0.34 ± 0.02	$0.85^{+0.13}_{-0.14}$	148^{+19}_{-21}	$1.63^{+0.07}_{-0.05}$	7.55	1.98	83	1.66	498/478
02	1.4 ± 0.2	10.5 ± 0.2	1.36 ± 0.02	$0.35^{+0.02}_{-0.01}$	0.95 ± 0.10	203^{+21}_{-19}	2.12 ± 0.06	9.00	2.30	83	1.67	528/493
03	$1.6^{+0.1}_{-0.2}$	$11.1^{+0.2}_{-0.1}$	$1.55^{+0.03}_{-0.04}$	0.32 ± 0.02	0.85 ± 0.11	182^{+22}_{-17}	$1.81^{+0.05}_{-0.04}$	8.28	2.34	73	1.66	527/506
04	$2.1^{+0.1}_{-0.2}$	$9.86^{+0.19}_{-0.24}$	$1.49^{+0.03}_{-0.07}$	$0.41^{+0.02}_{-0.03}$	0.93 ± 0.12	167^{+23}_{-17}	$2.16^{+0.09}_{-0.06}$	10.45	3.86	73	1.69	515/493
05	$1.7^{+0.2}_{-0.3}$	$13.0^{+0.5}_{-0.6}$	$1.21^{+0.05}_{-0.04}$	0.21 ± 0.02	$0.51^{+0.21}_{-0.23}$	81^{+18}_{-17}	$1.17^{+0.05}_{-0.02}$	4.62	0.31	101	1.63	60/73
06	1.6 ± 0.2	$13.0^{+0.4}_{-0.5}$	$1.29^{+0.03}_{-0.07}$	0.20 ± 0.01	$0.47^{+0.18}_{-0.20}$	90^{+18}_{-16}	$1.01^{+0.04}_{-0.03}$	4.02	0.29	95	1.63	372/402
07	$1.5^{+0.2}_{-0.3}$	12.5 ± 0.4	$1.27^{+0.13}_{-0.08}$	0.25 ± 0.02	0.64 ± 0.18	108 ± 21	$1.42^{+0.06}_{-0.08}$	5.85	0.76	95	1.64	366/415
08	1.6 ± 0.2	$12.2^{+0.4}_{-0.3}$	1.42 ± 0.03	0.23 ± 0.02	$0.56^{+0.18}_{-0.19}$	106^{+20}_{-19}	$1.37^{+0.04}_{-0.05}$	5.45	0.65	84	1.64	401/415
09	$1.9^{+0.2}_{-0.3}$	$12.7^{+0.3}_{-0.2}$	$1.44^{+0.03}_{-0.07}$	0.27 ± 0.02	$0.72^{+0.20}_{-0.19}$	110^{+27}_{-18}	$1.40^{+0.06}_{-0.04}$	6.11	0.98	84	1.64	348/415
10	$1.4^{+0.4}_{-0.3}$	$11.5^{+0.7}_{-0.4}$	$1.17^{+0.13}_{-0.03}$	$0.26^{+0.02}_{-0.03}$	$0.55^{+0.19}_{-0.25}$	103^{+21}_{-26}	$1.37^{+0.05}_{-0.08}$	4.97	0.40	101	1.66	301/334
11	$3.7^{+0.1}_{-0.3}$	$12.3^{+0.4}_{-0.7}$	$1.22^{+0.10}_{-0.05}$	$0.27^{+0.03}_{-0.02}$	$0.07^{+0.56}_{-0.07}$	43^{+19}_{-10}	$1.38^{+0.07}_{-0.06}$	5.82	0.90	99	1.64	193/236
12	$3.6^{+0.4}_{-0.2}$	$12.3^{+1.1}_{-0.4}$	$1.22^{+0.18}_{-0.04}$	0.27 ± 0.03	$0.21^{+0.62}_{-0.21}$	46^{+21}_{-12}	$1.38^{+0.04}_{-0.06}$	5.78	0.85	99	1.64	201/238
13	2.5 ± 0.8	$13.4^{+0.6}_{-0.5}$	$1.47^{+0.06}_{-0.03}$	0.25 ± 0.02	$0.50^{+0.21}_{-0.22}$	88^{+21}_{-22}	$1.31^{+0.06}_{-0.07}$	5.96	0.91	83	1.62	365/411
14	1.7 ± 0.2	$13.0^{+0.5}_{-0.4}$	$1.37^{+0.13}_{-0.03}$	0.28 ± 0.02	$0.61^{+0.18}_{-0.19}$	109^{+20}_{-19}	$1.42^{+0.05}_{-0.06}$	6.35	0.96	89	1.63	391/415
15	$2.8^{+0.2}_{-0.4}$	$14.6^{+0.6}_{-0.8}$	$1.32^{+0.09}_{-0.08}$	0.23 ± 0.02	$0.42^{+0.34}_{-0.40}$	62^{+27}_{-17}	$1.14^{+0.07}_{-0.04}$	5.63	0.92	96	1.61	198/244
16	2.8 ± 0.2	14.0 ± 0.3	$1.49^{+0.02}_{-0.03}$	$0.30^{+0.01}_{-0.02}$	$0.41^{+0.17}_{-0.22}$	85^{+16}_{-15}	1.38 ± 0.04	6.67	1.02	84	1.62	436/402
17	3.3 ± 0.2	13.7 ± 0.5	$1.42^{+0.08}_{-0.13}$	0.22 ± 0.02	$0.37^{+0.30}_{-0.37}$	58^{+19}_{-15}	$1.11^{+0.05}_{-0.04}$	5.16	0.83	87	1.62	342/415
18	$2.0^{+0.1}_{-0.3}$	$9.53^{+0.40}_{-0.23}$	$1.59^{+0.04}_{-0.03}$	0.33 ± 0.02	$0.83^{+0.13}_{-0.12}$	150^{+32}_{-16}	$1.70^{+0.07}_{-0.06}$	7.34	2.47	67	1.69	481/489
19	$2.0^{+0.2}_{-0.3}$	$10.4^{+0.1}_{-0.3}$	$1.66^{+0.01}_{-0.05}$	0.29 ± 0.02	$0.86^{+0.13}_{-0.15}$	148^{+22}_{-21}	$1.34^{+0.06}_{-0.03}$	6.10	1.99	66	1.67	455/502
20	1.9 ± 0.2	$9.93^{+0.43}_{-0.18}$	$1.49^{+0.03}_{-0.06}$	$0.31^{+0.01}_{-0.02}$	0.85 ± 0.13	151^{+19}_{-20}	$1.47^{+0.04}_{-0.05}$	6.30	1.95	73	1.69	467/502
21	1.7 ± 0.2	$9.73^{+2.14}_{-1.38}$	$1.31^{+0.25}_{-0.36}$	$0.30^{+0.04}_{-0.06}$	0.82 ± 0.14	139 ± 20	$1.64^{+0.30}_{-0.46}$	6.47	1.73	84	1.69	47/73
22	1.3 ± 0.2	$8.70^{+2.75}_{-1.41}$	$1.08^{+0.32}_{-0.26}$	$0.34^{+0.05}_{-0.06}$	$0.76^{+0.13}_{-0.12}$	160^{+30}_{-20}	$1.98^{+0.39}_{-0.47}$	6.82	1.59	99	1.71	44/73
23	1.2 ± 0.3	$7.25^{+2.36}_{-0.56}$	$0.97^{+0.31}_{-0.42}$	0.39 ± 0.04	0.80 ± 0.12	171^{+22}_{-21}	$2.29^{+0.34}_{-0.46}$	6.32	1.11	103	1.75	43/73
24	$0.7^{+0.3}_{-0.1}$	$6.61^{+0.37}_{-0.31}$	$1.42^{+0.09}_{-0.05}$	$0.49^{+0.06}_{-0.04}$	$0.89^{+0.08}_{-0.11}$	301^{+22}_{-39}	$1.15^{+0.06}_{-0.09}$	5.03	2.55	66	1.78	379/409
25	$0.5^{+0.2}_{-0}$	$6.06^{+0.73}_{-0.67}$	$1.47^{+0.20}_{-0.22}$	$0.63^{+0.12}_{-0.09}$	$0.88^{+0.08}_{-0.07}$	346^{+26}_{-27}	$1.17^{+0.07}_{-0.14}$	4.28	2.22	62	1.80	354/409
26	$0.5^{+0.2}_{-0}$	$5.29^{+1.47}_{-1.15}$	$1.30^{+0.38}_{-0.29}$	$0.59^{+0.08}_{-0.06}$	0.93 ± 0.07	348 ± 27	$1.32^{+0.35}_{-0.28}$	3.69	1.70	67	1.83	52/67
27	$1.0^{+0.3}_{-0.2}$	$6.86^{+0.98}_{-0.78}$	$1.28^{+0.23}_{-0.17}$	$0.46^{+0.06}_{-0.05}$	$0.91^{+0.10}_{-0.11}$	263^{+28}_{-29}	$1.48^{+0.21}_{-0.14}$	4.21	1.39	76	1.77	380/409
28	0.8 ± 0.2	$6.63^{+0.36}_{-0.31}$	$1.43^{+0.08}_{-0.05}$	$0.50^{+0.05}_{-0.04}$	$0.90^{+0.08}_{-0.11}$	299^{+23}_{-35}	$1.14^{+0.07}_{-0.09}$	3.31	1.20	66	1.78	379/409
29	0.9 ± 0.2	$6.51^{+0.77}_{-0.39}$	$1.14^{+0.05}_{-0.06}$	$0.47^{+0.04}_{-0.05}$	0.91 ± 0.10	264 ± 27	$1.51^{+0.13}_{-0.17}$	3.74	1.01	83	1.78	388/409
30	0.6 ± 0.1	$3.68^{+0.81}_{-0.79}$	$0.86^{+0.49}_{-0.14}$	$0.75^{+0.09}_{-0.07}$	$0.93^{+0.08}_{-0.07}$	324^{+26}_{-23}	$2.17^{+0.65}_{-0.73}$	3.91	1.58	89	1.91	49/67
31	1.0 ± 0.2	$7.26^{+0.47}_{-0.41}$	$1.15^{+0.14}_{-0.12}$	0.38 ± 0.04	0.85 ± 0.11	228^{+26}_{-25}	$1.53^{+0.11}_{-0.15}$	3.86	0.84	87	1.75	388/409
32	1.8 ± 0.2	$10.4^{+0.3}_{-0.6}$	$1.47^{+0.04}_{-0.13}$	0.29 ± 0.02	$0.69^{+0.15}_{-0.16}$	128^{+22}_{-21}	$1.19^{+0.11}_{-0.04}$	4.03	0.75	76	1.67	388/409
33	$1.4^{+0.2}_{-0.4}$	$8.26^{+1.38}_{-0.82}$	$1.24^{+0.19}_{-0.20}$	$0.35^{+0.04}_{-0.05}$	$0.69^{+0.18}_{-0.15}$	151^{+38}_{-21}	1.63 ± 0.21	4.44	0.81	83	1.72	62/67
34	1.0 ± 0.3	$7.18^{+1.54}_{-0.83}$	$1.08^{+0.25}_{-0.16}$	$0.34^{+0.03}_{-0.05}$	$0.66^{+0.17}_{-0.16}$	160^{+30}_{-26}	$1.66^{+0.10}_{-0.30}$	3.65	0.46	92	1.75	42/67
35	0.9 ± 0.2	$7.48^{+1.20}_{-0.87}$	$1.13^{+0.21}_{-0.15}$	$0.36^{+0.05}_{-0.04}$	0.70 ± 0.11	189^{+23}_{-22}	$1.74^{+0.23}_{-0.24}$	4.15	0.63	89	1.75	41/67
36	1.1 ± 0.4	$8.15^{+1.22}_{-1.33}$	$1.16^{+0.17}_{-0.29}$	$0.38^{+0.07}_{-0.05}$	$0.78^{+0.12}_{-0.11}$	203^{+26}_{-25}	$1.56^{+0.31}_{-0.21}$	4.21	0.74	89	1.73	58/64
37	$2.3^{+1.0}_{-0.9}$	$7.27^{+2.05}_{-1.28}$	$1.14^{+0.35}_{-0.24}$	$0.45^{+0.08}_{-0.06}$	$0.79^{+0.19}_{-0.18}$	149^{+29}_{-27}	$1.54^{+0.35}_{-0.18}$	5.72	2.16	88	1.75	41/62
38	2.2 ± 0.9	$7.26^{+1.12}_{-1.02}$	$1.11^{+0.20}_{-0.19}$	$0.49^{+0.08}_{-0.06}$	$0.79^{+0.16}_{-0.13}$	169^{+25}_{-24}	$1.60^{+0.34}_{-0.25}$	4.58	1.32	89	1.75	45/62

[a]Hydrogen column density, in units of 10^{22} cm^{-2}. [b]Normalization of the thermal EQPAIR model component. [c]The unabsorbed total model flux (without reflection) in units of 10^{-8} erg cm^{-2} s^{-1}. [d]The unabsorbed model flux from the non-thermal component, in units of 10^{-8} erg cm^{-2} s^{-1}. [e]Temperature of the emitting plasma in keV (for the thermal EQPAIR component). [f]Photon spectral index of the thermal EQPAIR component in the 2–10 keV range.

flux without spectral slope change and pivoting at ∼50 keV, which produces anticorrelation of the fluxes in the soft and hard parts of the spectrum. However, these instruments do not provide detailed spectral information, giving fluxes only in some energy intervals. The effective photon spectral indices using fluxes in two energy bands and calculated in the wide (20–300 keV) energy interval, where real spectra experience a cut-off, should be treated with caution. Now it is possible to check the results of Zdziarski et al. (2002) using our set of observations, on which we have detailed spectral information in the wide energy

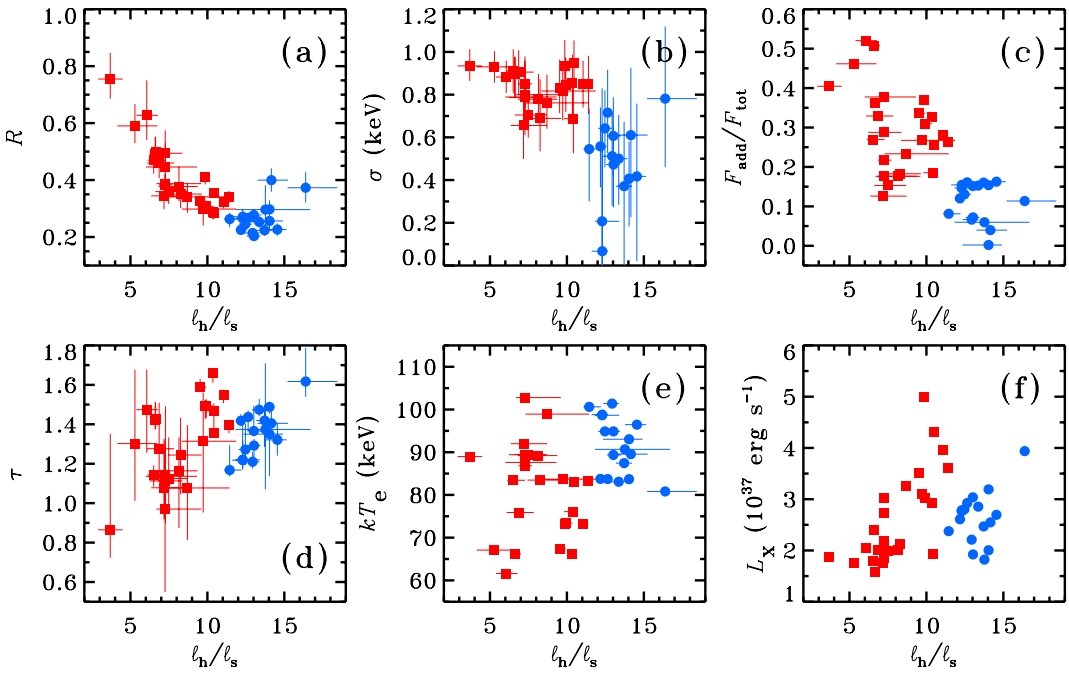

Figure 6. Dependences of the spectral parameters for model 2 (Section 3.2.4) fitted to the 1991 and 1997 (blue filled circles) and the 1996, 1998 and 1999 data (red filled squares) on the Compton amplification factor of the main Comptonization component $\ell_{\rm h}/\ell_{\rm s}$. The meaning of the axes is the same as in Fig. 4, except (c) the ratio of the additional non-thermal Comptonization flux in model 2 to the total flux.

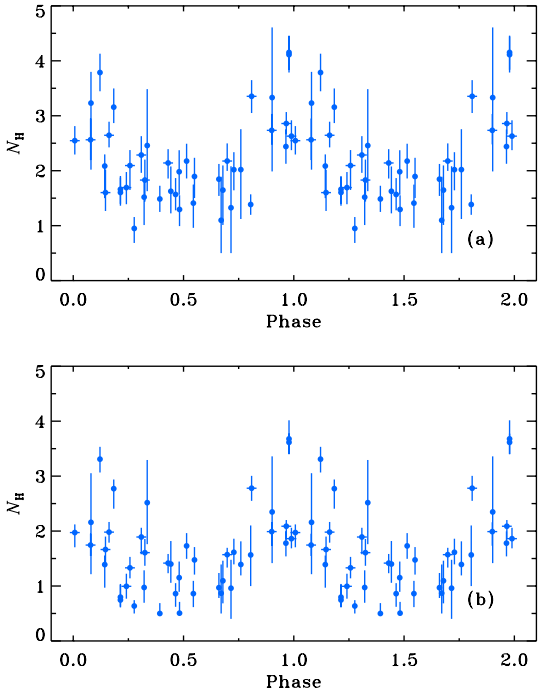

Figure 7. (a) Fitted value of absorption column density $N_{\rm H}$ for model 1 versus orbital phase of the binary system. (b) Same, for model 2. Distributions are repeated twice for clarity. $N_{\rm H}$ is in units of 10^{22} cm^{-2}.

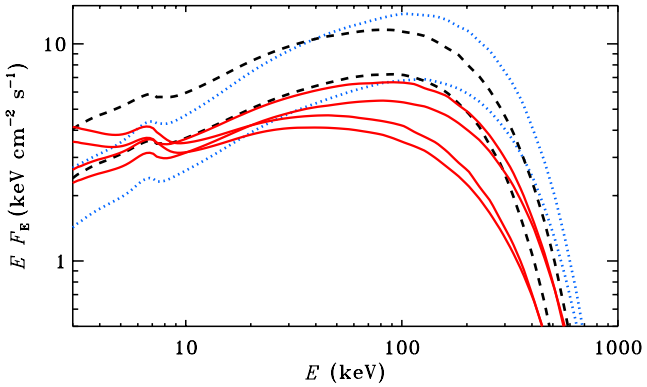

Figure 8. Sample of the spectra from different periods. Lowest and highest spectra from each time period are shown: red solid lines, 1999; blue dotted lines, 1991 (the 1997 spectra are similar to them); black dashed lines, 1996 and 1998. The 1991+1997 and 1996+1998 data form two groups with slightly different spectral slopes.

range. For this purpose, we use the model spectra obtained from model 1.

In Fig. 8 we present the spectra related to different time periods. It is possible to see that 1991, 1996–1998 spectra only change their normalization. However, the spectral slope is different for various years and forms two groups: 1991 + 1997 and 1996 + 1998 spectra. In the 1999 data, we can again see normalization changes (see pairs of red solid curves) as well as pivoting behaviour.

The Γ–flux correlations are shown in Fig. 9. It is clearly seen that the 1991 and 1996–1998 data do not show dependence between flux and Γ. The 1999 data show clear anticorrelation between Γ and flux at low energies (3–12 keV) and correlation at high energies (20–100, 100–300 keV), which indicates the pivoting behaviour with the pivot energy between 12 and ∼50 keV. In Fig. 9(d) (see also fig. 8 in Zdziarski et al. 2002), it can be seen that spectra from 1996 and 1998 are somewhat softer at high energies than the hard-state spectra from 1991 and 1997, but the fluxes in all energy intervals generally correlate with each other. The 1999 spectra show clearly different dependence: the high-energy fluxes are corre-

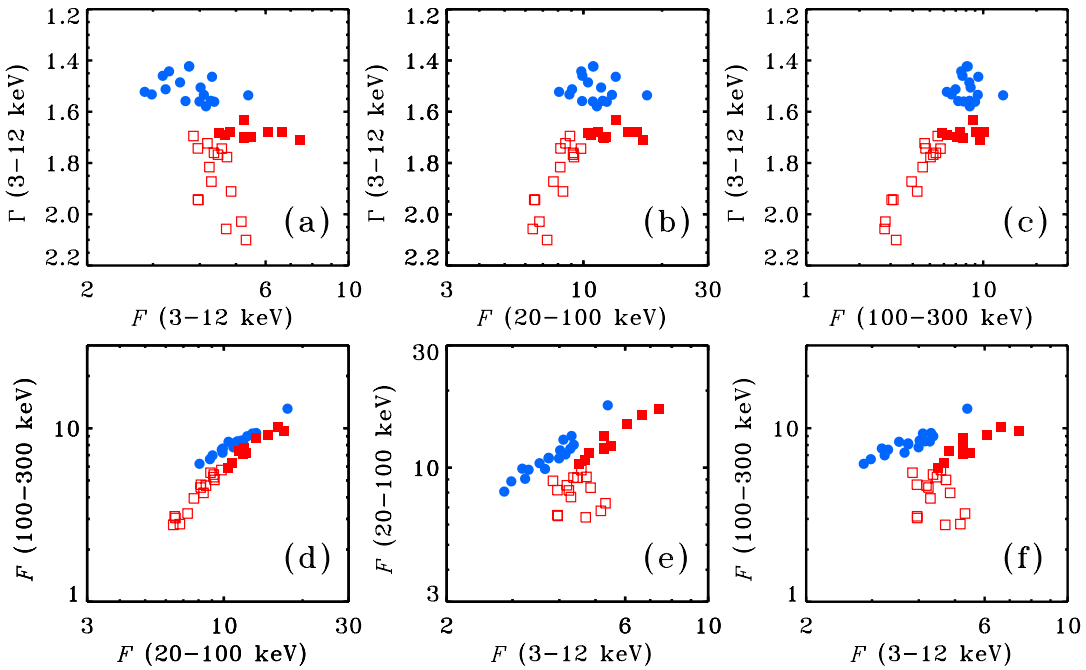

Figure 9. Flux–spectral index (3–12 keV) and flux–flux correlations. Respective energy intervals are indicated along the axis. The 1991 and 1997 data are indicated by blue filled circles, 1996 and 1998 by red filled squares, and 1999 by red open squares. All fluxes are in units of keV cm^{-2} s^{-1}.

lated, but there is a clear anticorrelation between 3–12 and 100–300 keV fluxes due to pivoting. The timing behaviour has also changed its nature in late 1998, as was pointed out by Pottschmidt et al. (2003).

4.3 Quasi-periodic oscillation frequencies

Among the data sets we have studied, there are timing data for 33 observations available from the recent paper by Axelsson, Borgonovo & Larsson (2005). This allows us to check the relation between the characteristic frequencies in the power density spectra and the spectral parameters. In the work of Axelsson et al. (2005), several values of QPO frequencies $\nu_{\rm QPO}$ might be determined during one observation, and for these data points we assume the averaged middle frequency and consider the uncertainty from lower to higher of obtained values. In agreement with the earlier results of GCR99, we find a clear anticorrelation between the characteristic frequencies of the aperiodic variability and $\ell_{\rm h}/\ell_{\rm s}$ (Fig. 10), indicating an apparent connection between QPO frequencies and the parameters of the Comptonizing region. This provides an argument (but not a proof) in favour of the presence of a hot inner corona and a variable inner radius of the surrounding disc.

The frequency–hardness correlation can be described by a power law $\nu_{\rm QPO} \propto (\ell_{\rm h}/\ell_{\rm s})^{-\alpha}$ with $\alpha = -1.48 \pm 0.04$. The best fit is shown by the solid curve in Fig. 10. A similar correlation was observed by Pottschmidt et al. (2003) and Nowak, Wilms & Dove (2002).

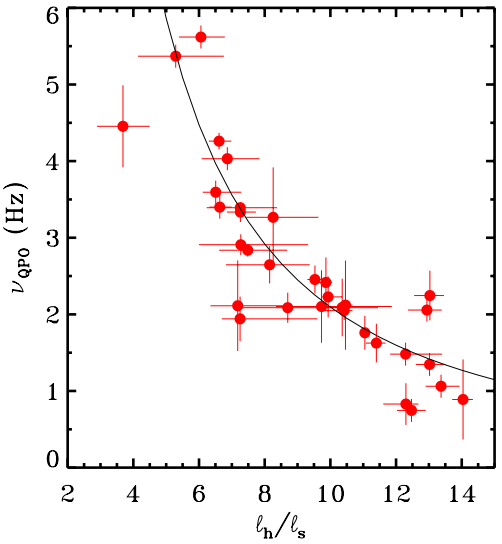

Figure 10. Dependence between QPO frequencies and $\ell_{\rm h}/\ell_{\rm s}$. The $\ell_{\rm h}/\ell_{\rm s}$ are best-fitting values from model 2. The QPO frequencies are from Axelsson et al. (2005). The solid curve shows the best power-law fit $\nu_{\rm QPO} \propto (\ell_{\rm h}/\ell_{\rm s})^{-1.48}$.

4.4 Comparison between phenomenological and physical spectral models and *R*–Γ correlation

Fig. 11 compares the results obtained with the simple phenomenological model of power law + reflection in the 3–20 keV energy range (model 0) with those from our model 2 applied to the 3–1000 keV range. More elaborate and physically justified models utilizing the full energy range of our data do not change the picture qualitatively. On the quantitative level, we find that the simple power law + reflection spectral fits to the 3–20 keV data overestimated the amplitude of the reflected component R and the slope Γ of the primary Comptonization continuum. We confirm, however, that the simple models did correctly rank the spectra according to the strength of the reflected component and slope of the Comptonized radiation, as demonstrated in the original publications on this subject (GCR99; ZLS99). This is also illustrated by the lower three panels of Fig. 11. The difference of the obtained parameters comes from the fact that, for wide-energy observations, the main thermal

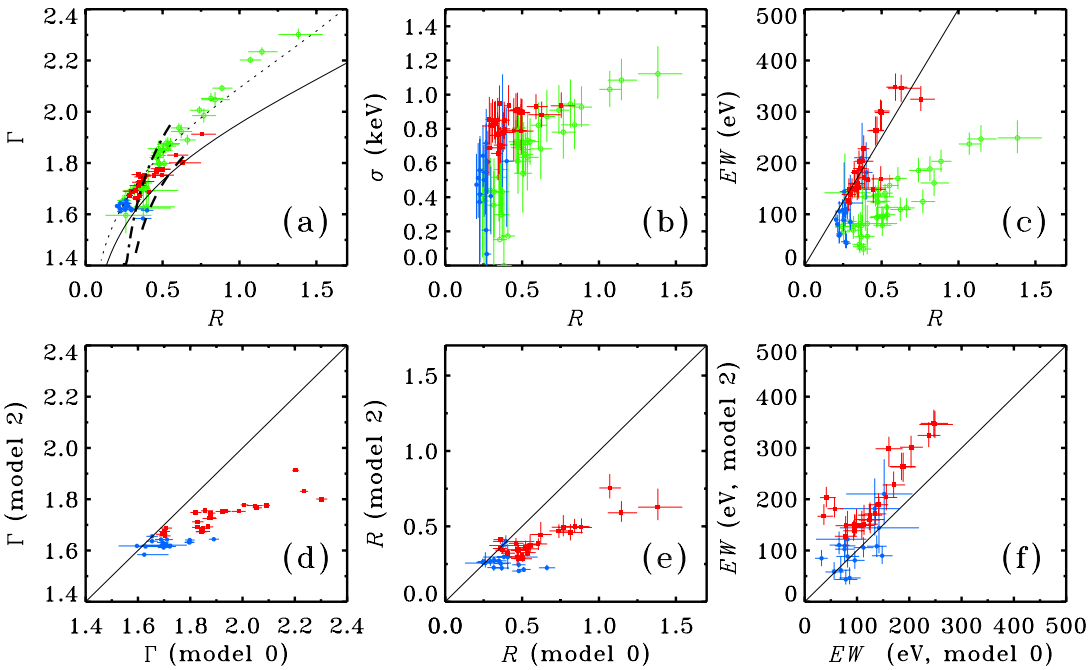

Figure 11. (a)–(c) Correlations obtained using model 0 (green open circles), model 1 (blue filled circles) and model 2 (red filled squares). (a) The spectral slope Γ versus reflection scaling factor R correlation. For model 0, Γ is a fitting parameter, for model 2 the index of a power-law fitted to the spectral model in the 2–10 keV range. The solid curve shows the dependence predicted for the ejection model (Beloborodov 1999a; MBP01) with the parameters of $i = 50^\circ$, the albedo of 0.15, $\mu_s = 0.5$ and $\tau = 2$, the dotted curve shows the same for $\mu_s = 0.4$. The dashed curve shows the dependence predicted by the model with a hot spherical corona and cold overlapping disc (Poutanen et al. 1997; ZLS99) with the blackbody temperature of 0.2 keV (see Section 4.4 for details). The dot-dashed curve shows the same model with the dissipation effect taken into account (dissipation parameter $L_{\rm int} = 1$, $L_{\rm int}/4\pi = 1$ at $r < 1$; see Appendix A for details). (b) The relativistic smearing Gaussian width σ at 6.4 keV versus R. (c) The equivalent width of the 6.4-keV line equivalent width versus R. The straight line is EW (eV) $= 500R$. (d)–(f) Γ, R and equivalent width obtained from model 2 versus those from model 0.

Comptonization component that describes well the hard energy tail may lie well below the observed flux in the 2–10 keV range (see Figs 3 and 5) and has a different slope in this band. The difference is largest for 1996, 1998 and 1999 data, while in the 1991 and 1997 cases the soft excess is weak and parameters obtained with the physical models are similar to those obtained with the phenomenological models.

In Fig. 11(a), we see a clear correlation between Γ and R. For comparison, we also show the dependences predicted by the plasma ejection model of Beloborodov (1999a,b) and MBP01 (cylindrical geometry with $h/r = 2$), using the geometric parameter of that model of $\mu_s = 0.4$ and 0.5, $i = 50^\circ$, the albedo of the reflecting medium of 0.15 and $\tau = 2$. We used the dependence between the amplification factor A of Comptonization and Γ from MBP01. We also compared our data with the dependence expected in the model of ZLS99, assuming the blackbody temperature of 0.2 keV, appropriate for Cyg X-1, with one minor change. In the original paper, all the reflection luminosity was assumed to reach the observer. Reflection amplitude is an integral that consists of two parts, from the disc inside the corona and from the outer part of it. We multiplied the part of luminosity coming from the former part by $e^{-\tau}$, to approximately take into account scattering of radiation in the corona ($\tau = 1$ was chosen). We see that this model cannot quantitatively describe the presented data. Moreover, taking into account intrinsic dissipation in the disc (see Appendix A for details) will further increase the slope of the dependence, making the discrepancy larger. Intrinsic dissipation becomes important for a small inner disc radius (when reflection is relatively large) and the increase of the soft seed photon flux in that case makes the spectrum softer (see Beloborodov 2001).

4.5 Physical scenario

The hard spectral state of BHBs is commonly defined as the state in which the spectrum is dominated by the hard Comptonization component, without significant contribution of the blackbody-type emission from the optically thick accretion disc. Naturally, the hard state is not characterized by a single, uniquely defined spectrum, but rather includes a continuum of spectral shapes with the major spectral parameters varying in a rather broad range. The diversity of the hard-state spectra reflects the position of the source with respect to the 'bottom hard' state and the soft state. Quantitatively, this position can be characterized by the strength of the reflected component (reflection scaling factor R or Fe line equivalent width) or properties of the main Comptonized component (Comptonization parameter, or Compton amplification factor $A = \ell_h/\ell_s$, or the photon index Γ in the low-energy limit) or characteristic frequencies of the aperiodic variability. The existence of good correlations between all these quantities suggests that they all are an equally good measure of the source position within the hard state. The results found in earlier work (GCR99; ZLS99; Gilfanov et al. 2000; Gilfanov, Churazov & Revnivtsev 2004) and presented in the previous sections of this paper suggest the following pattern of spectral and temporal variability. An increase of the strength of the reflected component is accompanied by an increase of the width of the Fe line, an increase of the characteristic QPO frequencies and a softening of the Comptonized component observed as an increase of its photon index Γ in the low-energy limit.

We find from our spectral analysis that in the 'bottom hard' state the broad-band spectrum (3–1000 keV) is mostly described by the single thermal Comptonization spectrum with superimposed

component due to reflection of the primary emission from relatively cool and neutral, or partly ionized, optically thick matter (the accretion disc), with an additional relatively weak soft component. As the source moves towards the soft state, the strength of the reflected component increases, and the soft component becomes more significant. Considering the 3–1000 keV energy range covered by our data, this spectral component reveals itself most clearly in the $E \lesssim 10$ keV energy domain as the 'soft excess'. Another independent indication of spectral complexity is the gamma-ray power-law tail detected at MeV energies by the COMPTEL telescope (McConnell et al. 2002).

From the point of view of the formal fit quality, the $E \lesssim 10$ keV excess can be described equally well by an additional thermal Comptonization component due to low temperature, low Comptonization parameter plasma or by non-thermal Comptonization with the power-law index of accelerated electrons $\Gamma_{\rm inj} \sim 2$–3. Owing to the complex shape of the continuum at these energies defined by the superposition of several spectral components, these two possibilities cannot be easily discriminated based solely on the low-energy data. The task is further complicated by the rather limited low-energy coverage provided by the PCA instrument, $E > 3$ keV. However, the above possibilities predict very different behaviour in the ∼MeV energy domain, where the main thermal Comptonization component diminishes and the power-law tail due to the non-thermal Comptonization should reveal itself. As the OSSE sensitivity and energy range are insufficient to probe the existence of the MeV tail correlated with the $E < 10$ keV excess, we cannot, strictly speaking, give preference to either of these two models.

There are however several additional considerations to be taken into account. (i) COMPTEL detected a weak MeV tail in the averaged hard-state data for Cyg X-1 (McConnell et al. 2002). The slope and amplitude of this tail are qualitatively consistent with the extrapolation of the non-thermal Comptonized component, required to explain the $E \lesssim 10$ keV excess (Fig. 5). (ii) In the soft state, the non-thermal power law is the dominant (the only) high-energy component. (iii) The $E \lesssim 10$ keV excess is more pronounced in the spectra characterized by large reflection and the rather steep slope of the main Comptonized component, i.e. in those sufficiently close to the soft state. Its strength seems to increase with the increase of the reflection. These arguments suggest that the non-thermal origin of the $E \lesssim 10$ keV excess is more plausible. We note that the 1991 and 1997 data show much weaker excess. This may be explained by the lower relative luminosity of the non-thermal Comptonization component, which therefore reveals itself at lower energies, below the $E = 3$ keV threshold of the PCA instrument, but can be detected by instruments which have a response at lower energies, i.e. *BeppoSAX* (see Di Salvo et al. 2001; Frontera et al. 2001).

The overall qualitative picture can be outlined as follows. The overall geometry of the accretion flow is adequately represented by the truncated disc model with the inner radius of the standard optically thick geometrically thin disc varying from $\sim 6R_{\rm g}$ to $\sim$ several tens of $R_{\rm g}$. Inside this radius, the accretion flow proceeds via quasi-spherical optically thin hot flow. The plausible mechanism governing the transition from the disc accretion to the coronal flow is the disc evaporation process as proposed by Meyer & Meyer-Hofmeister (1994). The geometrically thin disc gives rise to the soft blackbody-type component. In addition, due to dynamo, solar-type magnetic flares can be produced above the accretion disc (Galeev et al. 1979). The electrons there can be accelerated and form non-thermal distribution. Comptonization of the disc emission on these electrons results in the power-law-like Comptonized emission. The inner optically thin flow gives rise to the thermal Comptonization component. The relative contributions of non-thermal and thermal Comptonized components are defined by the fractions of the gravitational energy released in the disc (i.e. outside $R_{\rm in}$) and in the inner hot flow (inside $R_{\rm in}$). The position of the transition radius is defined by the mass accretion rate and is modified by the irradiation-related effects. The transition radius decreases as the mass accretion rate increases.

The QPOs are due to some processes in the transition region near $R_{\rm in}$ and approximately scale with the Keplerian frequency and other characteristic time-scales of the coronal flow and standard accretion disc in the transition region.

The configuration with the large inner disc radius, probably $R_{\rm in} \gtrsim 50$–$100R_{\rm g}$, corresponds to the classical hard state. The main features of this 'bottom hard' state are low strength of the reflected continuum, relatively narrow fluorescent Fe line of small equivalent width, large Comptonization parameter of the thermal Comptonized component (hard spectra with the low-energy photon index $\Gamma \sim 1.6$), and low frequencies of QPOs. As only a small fraction of the gravitational energy is released in the disc, the contribution of the non-thermal component is small and the spectrum is adequately described by thermal Comptonization.

As the mass accretion rate increases, the transition radius decreases, and the disc moves towards the compact object. This results in an increase of the reflection, broader fluorescent Fe line, larger QPO frequencies, and smaller $\ell_{\rm h}/\ell_{\rm s}$, i.e. a smaller Comptonization parameter in the inner hot flow. The contribution of the non-thermal component increases. The optical depth of the thermal plasma of the inner flow decreases due the shrinking of the inner hot flow as the disc extends towards the compact object.

The classical soft state (we ignore all the complications and substates here) corresponds to the accretion disc extending all the way towards the last stable orbit or very close to it. Correspondingly, the inner hot flow disappears and the dominant or the only hard component is that due to non-thermal Comptonization of the disc emission on the non-thermal electrons accelerated in the magnetic loops/flares above the disc.

The behaviour of the temperature of the thermal Comptonization component is unclear. It seems relatively constant, which suggests the possible presence of electron–positron pairs (see MBP01).

The physical scenario qualitatively outlined above is based on the truncated disc picture and on the assumption that the spectral evolution is governed by the change of the transition radius between the standard accretion disc and the hot inner flow. In this picture, many of the observed correlations can be explained naturally. However, the R–Γ correlation is significantly better quantitatively explained by the non-stationary corona model (MBP01), in which the governing parameter is the velocity of the blobs of emitting plasma relative to the accretion disc. We note that both models are geometrical in their nature and the predicted qualitative relations between the physical parameters are obtained with a number of simplifying assumptions. Therefore, the results of quantitative comparison of the model predictions with the observed pattern of the spectral variability should be interpreted with caution and any conclusions regarding the validity of either model based on such a comparison would be premature.

5 CONCLUSIONS

Based on the broad-band (3–1000 keV) data from simultaneous observations by *Ginga* and *CGRO*/OSSE in 1991 and PCA and HEXTE instruments aboard *RXTE* and OSSE in 1996–1999 we have studied the spectral variability of Cyg X-1.

(i) We confirm earlier results on R–Γ correlation. Considering the 3–20 keV data, we find very tight one-parameter relations between reflection, spectral index and the width of the Fe line.

(ii) More elaborate and physically justified models utilizing the full energy range of our data do not change the picture qualitatively. On the quantitative level, we find that the simple power law + reflection spectral fits to the 3–20 keV data overestimated the amplitude of the reflected component R and the slope Γ of the primary Comptonization continuum. We confirm, however, that the simple models did correctly rank the spectra according to the strength of the reflected component and slope of the Comptonized radiation, as demonstrated in the original publications on this subject (GCR99; ZLS99).

(iii) Based on the analysis of the broad-band data, we found that the spectra in our sample can be adequately described by the thermal Comptonized component with superposed reflection from the optically thick disc and a soft excess. This excess is relatively weak in the case of the hardest spectra of our sample ($\Gamma \sim 1.7$). As the strength of the reflection increases, the excess becomes much more significant. The presence of this excess was the primary reason for the simple spectral approximations of the 3–20 keV data to overestimate both R and Γ. The nature of this excess cannot be unambiguously determined from our data. Based on the circumstantial evidence we suggest that it is the lower energy part of the non-thermal Comptonized component with the power-law index of accelerated electrons $\Gamma_{\rm inj} \sim 2$–3. At higher energies, this non-thermal component reveals itself as a power law detected by COMPTEL at MeV energies in the average hard state spectrum of Cyg X-1.

(iv) We note the variability of the absorption correlated with the phase of binary system. These results confirm previous findings of the X-ray dips in the source.

(v) The overall pattern of spectral and temporal variability can be summarized as follows. An increase of the strength of the reflected component is accompanied by an increase of the width of the Fe line, an increase of the characteristic QPO frequencies and a softening of the Comptonized component observed as an increase of its photon index Γ in the low-energy limit or, equivalently, a decrease of the Compton amplification factor $\ell_{\rm h}/\ell_{\rm s}$. Simultaneously, the optical depth of the thermal Comptonization decreases and the fractional contribution of the non-thermal component to the total energy flux increases. The exact behaviour of the electron temperature in the hot inner flow is not constrained by our data.

(vi) We suggest a qualitative physical scenario naturally explaining the observed behaviour. In this scenario, the evolution of the spectral parameters is governed by the value of the transition radius between the standard optically thick accretion disc and the inner quasi-spherical hot flow. The thermal Comptonized component originates in the inner hot flow as a result of Comptonization of the soft photons emitted by the accretion disc. The origin of the non-thermal component is related to the optically thick disc; for example, it can be produced due to non-thermal electrons accelerated near the surface of the optically thick disc in the solar-type magnetic flares. The relative contributions of non-thermal and thermal components to the total energy flux depend on the fractions of the gravitational energy of accreting matter released in the optically thick disc and in the hot inner flow.

ACKNOWLEDGMENTS

We are grateful to Bryan Irby (NASA/GSFC) for help with converting the *Ginga* data, and to Magnus Axelsson for sharing the results of the timing analysis. This work was supported by the Centre for International Mobility and the Väisälä foundation (AI), the Academy of Finland grants 201079 and 204600 and the Wihuri Foundation (JP), and the NORDITA Nordic project in High Energy Astrophysics. AI was also supported by RFFI 02-02-17174 and the presidential programme for support of leading scientific schools NSH-1789.2003.2. AAZ was supported by KBN grants PBZ-KBN-054/P03/2001, 1P03D01827 and 4T12E04727.

REFERENCES

Arnaud K. A., 1996, in Jakoby G. H., Barnes J., eds, ASP Conf. Ser. Vol. 101, Astronomical Data Analysis Software and Systems V. Astron. Soc. Pac., San Francisco, p. 17
Axelsson M., Borgonovo L., Larsson S., 2005, A&A, 438, 999
Balucińska M., Hasinger G., 1991, A&A, 241, 439
Balucińska-Church M., Belloni T., Church M. J., Hasinger G., 1995, A&A, 302, L5
Balucińska-Church M., Church M. J., Charles P. A., Nagase F., LaSala J., Barnard R., 2000, MNRAS, 311, 861
Beloborodov A., 1999a, ApJ, 510, L123
Beloborodov A., 1999b, in Poutanen J., Svensson R., eds, ASP Conf. Ser. Vol. 161, High Energy Processes in Accreting Black Holes. Astron. Soc. Pac., San Francisco, p. 295
Beloborodov A., 2001, Adv. Space Res., 28, 411
Bisnovatyi-Kogan G. S., Blinnikov S. I., 1977, A&A, 59, 111
Brocksopp C., Tarasov A. E., Lyuty V. M., Roche P., 1999, A&A, 343, 861
Coppi P. S., 1992, ApJ, 258, 657
Coppi P. S., 1999, in Poutanen J., Svensson R., eds, ASP Conf. Ser. Vol. 161, High Energy Processes in Accreting Black Holes. Astron. Soc. Pac., San Francisco, p. 375
Di Salvo T., Done C., Zycki P. T., Burderi L., Robba N. R., 2001, ApJ, 547, 1024
Done C., Mulchaey J. S., Mushotzky R. F., Arnaud K., 1992, ApJ, 395, 275
Ebisawa K., Ueda Y., Inoue H., Tanaka Y., White N. E., 1996, ApJ, 467, 419
Esin A. A., Narayan R., Cui W., Grove E. C., Zhang S.-N., 1998, ApJ, 505, 854
Feng Y. X., Cui W., 2002, ApJ, 564, 953
Frontera F. et al., 2001, ApJ, 546, 1027
Galeev A. A., Rosner R., Vaiana G. S., 1979, ApJ, 229, 318
Gierliński M., Zdziarski A. A., Done C., Johnson W. N., Ebisawa K., Ueda Y., Haardt F., Phlips B. F., 1997, MNRAS, 288, 958
Gierliński M., Zdziarski A. A., Poutanen J., Coppi P. S., Ebisawa K., Johnson W. N., 1999, MNRAS, 309, 496 (G99)
Gilfanov M., Churazov E., Revnivtsev M., 1999, A&A, 352, 182 (GCR99)
Gilfanov M., Churazov E., Revnivtsev M., 2000, in Zhao G., Wang J-J., Qiu H. M., Boerner G., eds, SGSC Conference Series, Vol. 1, Proceedings of the 5th Sino-German Workshop on Astrophysics, p. 114 (astro-ph/0002415)
Gilfanov M., Churazov E., Revnivtsev M., 2004, in Kaaret P., Lamb F. K., Swank J. H., eds, AIP Conf. Proc. 714, X-ray Timing: Rossi and Beyond. AIP, Melville, p. 97
Ichimaru S., 1977, ApJ, 214, 840
LaSala J., Charles P. A., Smith R. A. D., Balucinska-Church M., Church M. J., 1998, MNRAS, 301, 285
Li H., Miller J. A., 1997, ApJ, 478, L67
Ling J. C. et al., 1997, ApJ, 484, 375
McConnell M. L. et al., 1994, ApJ, 424, 933
McConnell M. L. et al., 2002, ApJ, 572, 984
Magdziarz P., Zdziarski A. A., 1995, MNRAS, 273, 837
Malzac J., Petrucci P.-O., 2002, MNRAS, 336, 1209
Malzac J., Beloborodov A., Poutanen J., 2001, MNRAS, 326, 417 (MBP01)
Matt G., 2001, in White N. E., Malaguti G., Palumbo G. G. C., eds, AIP Conf. Proc. 599, X-ray Astronomy. Stellar Endpoints, AGNs and the Diffuse X-ray Background. AIP, Melville, p. 209
Meyer F., Meyer-Hofmeister E., 1994, A&A, 288, 175
Meyer F., Liu B. F., Meyer-Hofmeister E., 2000, A&A, 354, L67

Miller K. A., Stone J. M., 2000, ApJ, 534, 398
Narayan R., Mahadevan R., Quataert E., 1998, in Abramowicz M. A., Björnsson G., Pringle J., eds, Theory of Black Hole Accretion Discs. Cambridge Univ. Press, Cambridge, p. 148
Nowak M. A., Wilms J., Dove J. B., 2002, MNRAS, 332, 856
Perola G. C., Matt G., Cappi M., Fiore F., Guainazzi M., Maraschi L., Petrucci P.-O., Piro L., 2002, A&A, 389, 802
Pottschmidt K. et al., 2003, A&A, 407, 1039
Poutanen J., 1998, in Abramowicz M., Björnsson G., Pringle J., eds, Theory of Black Hole Accretion Discs. Cambridge Univ. Press, Cambridge, p. 100
Poutanen J., Coppi P., 1998, Phys. Scr., T77, 57
Poutanen J., Svensson R., 1996, ApJ, 470, 249
Poutanen J., Krolik J. H., Ryde F., 1997, MNRAS, 292, L21
Revnivtsev M., Gilfanov M., Churazov E., 1999, A&A, 347, L23
Revnivtsev M., Gilfanov M., Churazov E., 2001, A&A, 380, 520
Różańska A., Czerny B., 2000, A&A, 360, 1170
Shakura N. I., Sunyaev R. A., 1973, A&A, 24, 337
Shapiro S. L., Lightman A. P., Eardley D. M., 1976, ApJ, 204, 187
Shimura T., Takahara F., 1995, ApJ, 445, 780
Sunyaev R. A., Titarchuk L. G., 1980, A&A, 86, 121
Sunyaev R. A., Trümper J., 1979, Nat, 279, 506
Svensson R., Zdziarski A. A., 1994, ApJ, 436, 599
Titarchuk L., 1994, ApJ, 434, 570
Tout C. A., Pringle J. E., 1992, MNRAS, 259, 604
Weaver K. A., Krolik J. H., Pier E. A., 1998, ApJ, 498, 213
Zdziarski A. A., Gierliński M., 2004, Progr. Theor. Phys. Suppl., 155, 99
Zdziarski A. A., Gierliński M., Gondek D., Magdziarz P., 1996, A&AS, 120, 553
Zdziarski A. A., Johnson W. N., Poutanen J., Magdziarz P., Gierliński M., 1997, in Winkler C., Courvoisier T. J.-L., Durouchoux Ph., eds, SP-382, The Transparent Universe, Proc. 2nd INTEGRAL Workshop. ESA Publications Division, Noordwijk, p. 373
Zdziarski A. A., Lubiński P., Smith D. A., 1999, MNRAS, 303, L11 (ZLS99)
Zdziarski A. A., Poutanen J., Paciesas W. S., Wen L., 2002, ApJ, 578, 357
Zdziarski A. A., Lubiński P., Gilfanov M., Revnivtsev M., 2003, MNRAS, 342, 355

APPENDIX A: DISSIPATION AND ATTENUATION IN THE DISC–HOT FLOW MODEL

ZLS99 have considered an idealized geometrical model for thermal Comptonization, reprocessing and reflection in an accretion flow consisting of a central hot sphere surrounded by a flat cold disc (see fig. 2 in ZLS99). The sphere has a unit radius, and the inner radius of the disc can assume any value, d. For $d < 1$, there is an overlap between the two components. The hot sphere Comptonizes soft seed photons emitted by the disc. In the original model of ZLS99, the disc reprocesses and re-emits only the photons emitted by the sphere incident on the disc.

Here, we generalize this model to include intrinsic dissipation in the cold disc (as expected in an accretion flow). Also, we take into account scattering of the Compton-reflected photons in the hot sphere, which was neglected in ZLS99. For completeness, we give here the full set of relevant equations, but refer the reader to ZLS99 for details of the derivation.

The hot sphere has a unit luminosity and emits isotropically. The total flux incident on the disc at a radius, r, is then given by (ZLS99)

$$F_{\rm inc}(r) = \frac{3h(r)}{16\pi^2}, \tag{A1}$$

where

$$h(r) = (4/3) \times \begin{cases} \left[(2-r^{-2})E(r^2) + (r^{-2}-1)K(r^2)\right], & r < 1, \\ \left[(2r-r^{-1})E(r^{-2}) + 2(r^{-1}-r)K(r^{-2})\right], & r \geqslant 1, \end{cases} \tag{A2}$$

where E and K are complete elliptic integrals. The luminosity of the disc due to re-emission of photons incident on it is

$$L_{\rm inc}(d) = 4\pi \int_d^\infty {\rm d}r\, r F_{\rm inc}(r). \tag{A3}$$

This can be divided into the contributions to the integral from the parts of the disc at $d \leqslant 1$ and $d > 1$, $L_{\rm inc} = L_{\rm inc}^{<} + L_{\rm inc}^{>}$, where the first term is non-zero only for $d < 1$.

Then, the relative strength of Compton reflection can be identified (ZLS99) with the ratio of the luminosity of the disc due to irradiation to the fraction of the sphere luminosity that is not incident on the disc. However, we correct here for attenuation of the reflection from the parts of the disc with $d < 1$ because of scattering by the hot electrons in the sphere. For the radial optical depth of the sphere τ, we can then write

$$R \simeq \frac{{\rm e}^{-\tau} L_{\rm inc}^{<} + L_{\rm inc}^{>}}{1 - L_{\rm inc}}. \tag{A4}$$

Another effect not included in the treatment of ZLS99 is the intrinsic dissipation in the disc. Far away from the centre (so any effect of the inner boundary condition is negligible), the dissipated flux per unit area is $\propto r^{-3}$, and we assume it for $r > 1$. On the other hand, the dissipation in the part of the disc inside the hot sphere, $r < 1$, is reduced due to the transfer of the power to the hot plasma. We assume here that dissipation is either null or constant matching that of the outside disc

$$F_{\rm int}(r) = \frac{L_{\rm int}}{4\pi} \begin{cases} 0 \ \text{ or } \ 1, & r \leqslant 1, \\ r^{-3}, & r > 1, \end{cases} \tag{A5}$$

where we parametrized the relative intrinsic dissipation by the dimensionless factor, $L_{\rm int}$, defined as the intrinsic luminosity of the disc extending from $r = 1$ to infinity (regardless of the actual value of d).

The power in seed photons scattered in the sphere from both the reprocessing and the intrinsic dissipation (assuming $\tau = 1$) is then

$$L_{\rm s}(d) \approx \frac{3(1-a)}{4\pi^2} \int_d^\infty {\rm d}r\, r h^2(r) + \frac{L_{\rm int}}{\pi} \int_{\max(d,1)}^\infty {\rm d}r\, \frac{h(r)}{r^2} + \frac{L_{\rm int}}{\pi} \int_d^1 {\rm d}r\, r h(r), \tag{A6}$$

where a is the albedo and the term given by the second line of equation (A6) appears only in the case of non-zero dissipation within the sphere and when $d < 1$.

The amplification factor of the process of thermal Comptonization is then $A(d) \equiv 1/L_{\rm s}(d)$. It can be related to the spectral index of the power-law part of the Comptonization spectrum using, for example, the formula of MBP01

$$\Gamma = C(A-1)^{-\delta}, \tag{A7}$$

where $C = 2.19$ and $\delta = 0.14$ for BHBs with $kT_{\rm seed} = 0.2$ keV.

This paper has been typeset from a TEX/LATEX file prepared by the author.